Published in final edited form as:

Curr Protoc. 2022 March ; 2(3): e379. doi:10.1002/cpz1.379.

Design, Construction, and Implementation of an MR Elastography (MRE) Actuator for Research Purposes

E.R. Triolo[1], **O. Khegai**[2], **E. Ozkaya**[2], **N. Rossi**[3], **A. Alipour**[2], **L. Fleysher**[2], **P. Balchandani**[2], **M. Kurt**[1,2,*]

[1]–University of Washington, Dept. of Mechanical Engineering (3900 E Stevens Way NE Seattle, WA 98195)

[2]–Icahn School of Medicine at Mount Sinai, BioMedical Engineering and Imaging Institute (1470 Madison Ave, New York City, NY 10029)

[3]–Stevens Institute of Technology, Dept. of Mechanical Engineering (1 Castle Point Terrace, Hoboken, NJ 07030)

Abstract

Magnetic resonance elastography (MRE) is a technique for determining the mechanical response of soft materials using applied harmonic deformation of the material and a motion sensitive magnetic resonance imaging (MRI) sequence. Use of this technique on human tissue (e.g. liver, brain) can elucidate significant information about its health and development, and this technique has been used on phantom models (e.g. Agar, silicone) to determine their suitability for use as a mechanical surrogate for human tissues in experimental models. The applied harmonic deformation used in MRE is generated by an actuator, transmitted in bursts of a specified duration and synchronized with the magnetic resonance (MR) signal excitation. These actuators are most commonly either a pneumatic design (common for human tissues or phantoms) or a piezoelectric design (common for small animal tissues or phantoms). Here, we describe how to design and assemble both a pneumatic MRE actuator and a piezoelectric MRE actuator for research purposes. For each of these actuator types, we discuss displacement requirements, end-effector options and challenges, electronic and electronic driving requirements and considerations, and full MRE implementation. We also discuss how to choose actuator type, size, and power based on intended material and use.

Basic Protocol 1: Design, Construction, and Implementation of a Convertible Pneumatic MRE Actuator for Use with Multiple Tissue Types

Basic Protocol 2: Design, Construction, and Implementation of a Piezoelectric MRE Actuator for Localized Excitation in Phantom Models

Keywords

Magnetic Resonance Elastography (MRE); Biomechanics; Magnetic Resonance Imaging (MRI)

[*]Corresponding Author. mkurt@uw.edu.

CONFLICT OF INTEREST STATEMENT:
The Authors declare no conflict of interest.

INTRODUCTION:

Historically, pathologies such as tumors or lesions have been identified by physicians by manually palpating soft tissue to compare mechanical properties of healthy tissue to potentially malignant tissues. However, for internal organs, such as the brain, this technique is not feasible. Therefore, it was necessary for a secondary method of producing these results, or even more accurate results, to be developed, such as Magnetic Resonance Elastography (MRE)(Hirsch et al., 2017; Muthupillai et al., 1996). Elastography is a technique for determining the mechanical response of a material using applied deformation of that material and a motion-sensitive imaging modality(Greenleaf et al., 1996). There are many different methods to apply the necessary force for tissue deformation in elastography, and magnetic resonance imaging (MRI) is a popular method of detection of the tissue deformation. In MRE, or the process of performing elastography using MRI, the most common form of recurrently deforming tissue in a controlled manner is through harmonic vibration(Greenleaf et al., 2000). Viscoelastic models are used to extract structural information from MRE measurements by establishing a mathematical relationship between the harmonic vibration applied and the resulting deformation of the tissue(Kurt et al., 2019; Kwon et al., 2009; Manduca et al., 2002; Papazoglou et al., 2012; Van Houten et al., 2001; M. Yin et al., 2007). Performing MRE on brain tissue can provide information on different structures within brain tissue based on their mechanical properties (*i.e.*, magnitude of the complex shear modulus, damping ratio), such as cell density, myelination, inflammation, and functional activation(Fehlner et al., 2014; Guo et al., 2013; Hiscox et al., 2018, 2020; Huston et al., 2015, 2016; Johnson et al., 2016; Kurt et al., 2019; McIlvain et al., 2018; Murphy et al., 2016; Pattison et al., 2009; Perry et al., 2017; Sack et al., 2009, 2011; Streitberger et al., 2011; Zhang et al., 2011). These mechanical parameters (*i.e.*, magnitude of the complex shear modulus, damping ratio) can then be used to diagnose pathologies such as multiple sclerosis (MS), Alzheimer's disease, and Parkinson's disease, or indicate disease progress(ElSheikh et al., 2017; Gerischer et al., 2016; Hiscox et al., 2019; Johnson et al., 2017; Lipp et al., 2013, 2018; Murphy et al., 2011, 2016; Streitberger et al., 2012; Wuerfel et al., 2010). Additionally, because tissue is viscoelastic, the mechanical response of tissue is dependent on loading speed, or in the case of MRE, the frequency of actuation. Therefore, some studies use multifrequency MRE, in which the vibration is applied and encoded at different frequencies to determine the viscoelasticity(Kurt et al., 2019; Lipp et al., 2013; Neumann, Lehnart, et al., 2018; E Ozkaya et al., 2021).

When performing MRE on any tissue type, harmonic vibration must be induced in the tissue in synchronization with the motion encoding gradient (MEG) (Hirsch et al., 2017; Muthupillai et al., 1996). This process requires a type of harmonic actuator that can be used to actuate tissue inside the MRI machine. Therefore, this actuator must be magnetic resonance (MR) compatible, or at least the part of the driver unit that is used inside the scanner room should be MR compatible. In general, there are three main categories of actuators. First, there are indirect actuators that use an active driver outside of the scanner room and a passive driver inside the scanner(Asbach et al., 2008; Chang et al., 2016; Chaze et al., 2019; Feng et al., 2018; Freimann et al., 2012; Gruwel et al., 2010; Latta et al., 2011; Meng Yin et al., 2008). In this type of actuator, usually pneumatic, an active driver that

generates the vibration is placed in the control room as opposed to in the scanner room, and a passive driver is placed inside the scanner, in contact with the tissue of interest(Asbach et al., 2008; Chang et al., 2016; Chaze et al., 2019; Feng et al., 2018; Freimann et al., 2012; Gruwel et al., 2010; Latta et al., 2011; Meng Yin et al., 2008). A long rod or tube is then used to transmit the vibration from the active driver to the passive driver(Asbach et al., 2008; Chang et al., 2016; Chaze et al., 2019; Feng et al., 2018; Freimann et al., 2012; Gruwel et al., 2010; Latta et al., 2011; Meng Yin et al., 2008). The Resoundant, a pneumatic MRE device, is used by clinicians to diagnose liver fibrosis without a tissue biopsy (*MR Elastography | Resoundant Inc.*, n.d.). The passive component of this device has also been altered in various studies investigating the human brain and phantoms(Badachhape et al., 2018; Chaze et al., 2019; Hiscox et al., 2018; Zheng et al., 2007). To the best of our knowledge, this is the only commercially available MRE actuator and has been extensively tested in various studies across different organ systems(Tse et al., 2009; Venkatesh et al., 2013). The advantage of using a pneumatic actuator is that custom built versions are inexpensive and have a simple design, and pneumatic actuators in general allow for precise control with good MR compatibility of the passive driver(Latta et al., 2011). However, these designs typically have phase lag and therefore difficulties in synchronization control due to the long transmission tubes or rods necessary to transmit vibration(Neumann, Lehnart, et al., 2018). These are typically the designs used for brain MRE due to their versatility and ability to produce large enough actuation amplitude(Chaze et al., 2019; Freimann et al., 2012; Sack et al., 2009).

A second category of actuator takes advantage of the static magnetic field by using an electromagnetic coil/coil(s) to induce vibration. Current passing through an electromagnetic coil results in an oscillating magnetic field. Based on Lorentz Law, if the surface normal vector of the coil is perpendicular to the static magnetic field of the MRI machine, a rotary motion is generated(Uffmann et al., 2001). This rotary motion is then transferred to the tissue using some type of vibration pad or bite-bar (for brain MRE)(Hamhaber et al., 2003, 2010; Liu et al., 2009; Sack et al., 2002; M. Suga et al., 2003; Uffmann et al., 2001). This type of design is inexpensive as well, and can be manufactured using standard metal machining equipment(Tse et al., 2009). Also, a wide range of frequencies and displacements can be produced by changing the thickness of wire, amount of current, number of coils, and radius of coils(Uffmann et al., 2001). However, this design is not commonly used anymore and, generally, the application of this design is limited due to the MRI safety challenges associated with its metallic structure. Two main drawbacks are also that the coil is mostly inflexible in terms of positioning, and the induced magnetic field can potentially cause artifacts in the image(Tse et al., 2009). The third category of actuator category uses an active vibrational component that directly interfaces with the tissue, as opposed to the previous two categories where the active component is a distance away from the tissue and relies on a rod, pad, or pillow to transmit vibration over a distance. For this type of actuator, the entire unit has to be MR compatible and small enough to attach to the tissue of interest. The units are usually driven by air pressureor piezoelectric crystals(Brauck et al., 2007; Gordon-Wylie et al., 2018; Meinhold et al., 2019; Namani et al., 2009; Neumann, Bichert, et al., 2018; Numano et al., 2013; E Ozkaya et al., 2021; Rossman et al., 2003; Runge et al., 2019; Uffmann et al., 2002; Z. Yin et al., 2017). The main drawback for this type of device is that

they are usually quite bulky and have difficulty in attaching to the tissue of interest(Tse et al., 2009). Typically, this type of actuator, particularly the piezoelectric actuators, are more commonly used for MRE of small animals or phantoms (Brauck et al., 2007; Meinhold et al., 2019; Namani et al., 2009; E Ozkaya et al., 2021; Rossman et al., 2003; Uffmann et al., 2002; Z. Yin et al., 2017).

There is currently a need for research specific MRE actuators for various tissue types at multiple field strengths. While there are other device design papers that describe a specific custom pneumatic actuator (*e.g.*, (Feng et al., 2018; Latta et al., 2011)) for research purposes, there are no papers that describe how to design, build, and implement an MRE actuator in general. In designing the MRE actuators used in our research lab, we encountered many questions and challenges regarding their design and construction. In this paper, we endeavor to answer such questions and provide guidance for other laboratories attempting to design and implement their own MRE system for research studies in tissue or phantom mechanics. We also aim to offer validation methods and part selection guidelines for various MRE actuator applications. Here, we describe how to design and assemble both a pneumatic MRE actuator and a piezoelectric MRE actuator using all commercially available electronic components for research purposes. For each of these actuator types, we discuss displacement requirements, end-effector options and challenges, electronic and electronic driving requirements, and considerations, and full MRE implementation. We also discuss how to choose actuator type, size, and power based on intended material and use.

BASIC PROTOCOL 1:

Design, Construction, and Implementation of a Convertible Pneumatic MRE Actuator for Use with Multiple Tissue Types

The objective of Basic Protocol 1 is to design, construct, and implement a convertible pneumatic MRE actuator for research purposes on multiple tissue types using all commercially available electronic components. This protocol can be utilized to develop an actuator for MRE of the human brain, other human tissue, or phantom. In this protocol, we specifically focus on construction of an end-effector for either distributed vibration at the surface of a phantom or for the brain, however, this research pneumatic actuator design can be used for most tissue types. To convert the device to be used on a different tissue type, the design of the tissue-contacting end effector can be altered. Additionally, while how to construct and implement a pneumatic actuator using specific electronic components is described in this protocol, in the event that requirements for the desired actuator are different or the components are not available for purchase in a particular location, how to select different components are also discussed.

Materials: A full description of each component as it appears in our configuration is listed next to the general component name in italics. These components can be replaced with those that perform the same function, as described in the protocol.

Active Actuation components: Rubber-coned Subwoofer in an enclosure: *MTX Audio Terminator Series TNE212D 1,200-Watt Dual 12-Inch Sub Enclosure*

Class-D Audio Power Amplifier: *Behringer Monitor Speaker And Subwoofer Part (NX3000)*

Signal generator*: RIGOL DG1022 Series Dual-Channel Function/Arbitrary Waveform Generator*

Appropriate cabling for active components:

- Banana to Speakon Male Speaker Wire Audio Adapter
- Eightwood 75ohm BNC Plug Male to 3.5MM Mono Male Coaxial Power Audio Cable 3 feet,
- MillSO Headphone Adapter (10 Feet) TRS 1/4 Male to 3.5mm Female Stereo Jack,
- Monoprice 75-ohm BNC Male connector BNC Cable - 10 Feet

Passive End Effector Components: Anycubic i3 Mega 3-D Printer (or similar machine)

Thermoplastic Polyurethane (TPU) 3-D Printer Filament: *Overture TPU Filament 1.75mm, 1kg Spool*

Polylactic Acid (PLA) 3-D Printer Filament: *eSUN PLA PRO (PLA+) 3D Printer Filament, 1kg Spool, 1.75mm, Gray*

Cyanoacrylate glue: *BSI MAXI-CURE Cyanoacrylate glue*

Stiff rubber tubing: *McMaster-Carr: Firm Clear Polyurethane Rubber Tubing for Drinking Water, Clear, 3/4" ID, 1–1/16" OD, 25 ft. Length (Catalog 5439K25)*

1/8" thickness acrylic sheet*: McMaster-Carr: Clear Scratch- and UV-Rst Cast Acrylic Sheet 48" X 48" X 1/8*

CNC machine, laser cutter, or jigsaw and power drill

Hex key set or screwdriver set (dependent on screws used on selected subwoofer)

Hot glue gun and hot glue or caulking silicone

Clamps

MRI-Compatible tape

MRI- Compatible adhesive bandage

Protocol Steps with *Step Annotations*

Component Selection

1. Select an appropriate rubber-coned subwoofer and corresponding Class-D audio power amplifier based on the intended use. The frequency response of the subwoofer and amplifier should be an appropriate range for the human tissue

being imaged, generally 45–80Hz for the heart(Arani, Glaser, et al., 2017; Barnhill et al., 2017; Rump et al., 2007; Wassenaar et al., 2016), 40–70Hz for the kidney or liver(Asbach et al., 2010; Dittmann et al., 2017; Etchell et al., 2017; Feng et al., 2018; Lee et al., 2012; Marticorena Garcia et al., 2018; Morisaka et al., 2017; Sack et al., 2013), 30–150Hz for skeletal muscle(Barnhill et al., 2013; Bensamoun et al., 2006; Hollis et al., 2016; Kennedy et al., 2020; Papazoglou et al., 2006; Sack et al., 2002, 2013; Mikio Suga et al., 2001), 40–60 for the pancreas(Dittmann et al., 2017; Shi et al., 2015, 2018), 65–300Hz for the breast(Hawley et al., 2017; Plewes et al., 2000; Van Houten et al., 2003), or 25–100Hz for the brain(Guo et al., 2013; Hamhaber et al., 2010; Hiscox et al., 2020; Johnson et al., 2016; Kurt et al., 2019; Efe Ozkaya et al., 2021; Xu et al., 2007; Zhang et al., 2011). The maximum power output of the audio amplifier should be greater than the maximum power handling of the subwoofer at the impedance of the subwoofer for obtaining the maximum amplitude the subwoofer is capable of outputting.

a. **Power and Impedance Selection Considerations:** For performing MRE of the human brain and a phantom, we selected a dual 12-inch sealed enclosure with a 1200W maximum power handling at 2ohms impedance (bottom component shown in Figure 2(a) and shown modified in Figure 2(b)), and a 2-channel class-D power amplifier with 1500W maximum deliverable power per channel at 2ohm impedance (top component shown in Figure 2(b)).

   Audio equipment typically has an impedance of 2ohms or 4ohms. Most equipment specifications of subwoofers list one or the other, but technical specifications of amplifier will list both, as they can usually amplify at either impedance. Note the impedance of the subwoofer to ensure that the correct specifications are being considered for the amplifier.

b. **Amplitude Selection Considerations:** In our configuration, while both cones are driven simultaneously, only one 12-inch cone is supplying air into the passive driver components. This amplitude is more than sufficient for applying vibration to a phantom material (less than half power selected on the amplifier) and sufficient for providing vibration to the human brain (between 2/3 to maximum power selected on the amplifier).

   For any speaker, the maximum volume of air that a cone can move, or its Peak Diaphragm displacement Volume can be calculated by multiplying twice the maximum linear excursion (Xmax) by the surface area of the cone (Sd). These two values can usually be found in the data sheet of the speaker or can be requested from the manufacturer. This would be a good starting point for determining cone size, and subsequently amplifier power, however, between the cone

and end-effector, there will be some loss due to dampening. The movement of the end-effector can be determined using a laser doppler vibrometer or an equivalent test (as described in 'Understanding Results'), which would give the most accurate calculation of the amplitude supplied by the actuator.

2. Select a signal generator capable of being triggered by an external time-to-live (TTL) signal to output a specified signal burst.

3. Select the appropriate cabling to connect the input of the subwoofer to the output of the amplifier, the input of the amplifier to the output of the signal generator, and the external TTL triggering input of the signal generator to the TTL trigger output of the MRI scanner.

    a. **Audio Cabling:** *Audio cabling is not standardized, so the cabling required is dependent on the components selected in steps 1 and 2. In our case, the TTL output of the MRI scanner and TTL triggering input of the signal generator requires a BNC male-BNC male cable, but this may differ between systems.*

    b. **Example Configuration Cabling Selection:** In our configuration, we utilized a male dual banana to male Speakon to connect the subwoofer to the amplifier, a 1/4" male to 3.5mm female and 3.5mm male to BNC male cables to connect the amplifier to the signal generator, and a BNC male to BNC male to connect the signal generator to the MRI scanner output.

4. Select firm, flexible tubing to connect the active components (selected in steps 1–3) to the tissue-contacting passive component. The tubing must be long enough to reach from the active components in the MRI equipment room, through the waveguide, and into the MRI scanner bore.

    The tubing should be flexible enough to make all necessary turns without necessitating connectors, but firm enough to not absorb and therefore dampen vibration along its length.

    a. **Example Configuration Tubing Selection:** In our configuration, we used 25ft of rm clear polyurethane rubber tubing of 3/4" inner diameter, with bend radius 3.5" and durometer 85A.

Building and Manufacturing

5. Using a CAD software, design a hollow end-effector based on the intended use. For phantom, the end-effector should be relatively the same size as the phantom's surface. For the brain, the end-effector should mimic the shape of the MRI scanner's head coil for patient comfort. For other tissue, the end-effector should be re-sized based on the tissue, and easily connectable to the tissue (Figure 3).

6. Using the 3-D printer, print the custom end-effector using TPU lament in such a way that the end-effector is hollow. This may necessitate printing the end-effector in multiple parts (Figure 4), then connecting them using cyanoacrylate glue, hot glue, and/or silicone, and clamping the pieces together until the glue/silicone is set.

    a. **End Effector Design Considerations:** Depending on the shape and thickness of the end-effector, internal supports may be necessary to prevent complete compression of the end-effector by the tissue. This is particularly of interest for the human head-contacting end-effector, as the full weight of the head is pressing on a particularly thin pillow. To overcome this, in our configuration, we insert the 3-D printer supports used to print the ‘cap’ portion of the end-effector into the center of the pillow before it is fully sealed (Figure 5).

    b. **End Effector Example Designs:** In our configuration, we 3-D print the end-effector in two main components, with multiple 3-D printed custom tubing segments 4. We attach these components with cyanoacrylate glue and seal these seams with hot glue to both maintain air pressure and add strength to the potentially vulnerable joins. Photos of this process can be found in Figure 5.

7. Using a CNC machine, laser cutter, or jigsaw and power drill, cut the acrylic sheet to match the shape and size of the front of the subwoofer with a small hole in the center, approximately the size of the tubing selected. Use the existing screws used to hold the subwoofer cone in its enclosure to attach the sheet to the front of the cone. This is to channel the air through the hole in the front of the disk of acrylic and maintain air pressure.

    a. Some subwoofer cones that are made of rubber have a raised portion next to the outside edge of the cone. To combat this, in our configuration, we also cut a ring from the acrylic sheet and attached it underneath the acrylic disk to raise the disk enough to not compress the raised part of the cone (Figure 6).

8. Using a CAD software, design a custom connector for attaching the tubing to the front of the acrylic sheet before 3-D printing the connector using PLA lament and attaching it to the sheet using cyanoacrylate glue, sealing the edges with hot glue (Figure 6).

Implementation and Testing

9. Place all the active components (aka the now modified subwoofer, the audio amplifier, the signal generator, and the associated cabling) in the MRI scanner equipment room. Subsequently, use the appropriate cabling to connect the TTL trigger output of the scanner to the ‘TTL external triggering’ port on the signal generator, the output of the signal generator to the ‘audio in’ on the audio amplifier, and the ‘subwoofer out’ on the audio amplifier to the input on the modified subwoofer (Figure 7).

The trigger output is the standard with the scanners used (3T Skyra and 7T Terra, Siemens Healthineers) and is the same for any other application that requires triggering. Some scanners (e.g., Siemens) uses a fiber-optic output which can be altered to any cable type using a media converter, while other scanners (e.g., Phillips) have a BNC TTL output directly. The signal itself is programmed in the pulse sequence (timing and duration of TTL signal) with Siemens IDEA pulse programming environment.

10. Connect one end of the flexible tubing to the custom 3-D printed connector on the modified subwoofer before feeding the other end of the tubing through the waveguide into the MRI scanner room. Subsequently, attach the custom end-effector to the end of the tubing that is now inside the scanner room using MRI-compatible tape. Using MRI-compatible tape instead of a glue makes it more convenient to switch out the end-effector so the same actuator can be used to apply vibration to a variety of tissues or phantoms. If a more permanent connection is desired, using glue prior to moving the tubing and end-effector into the MRI scanner room is also a viable option.

11. Turn on the signal generator and set the frequency to the desired vibration frequency and the peak to peak voltage (Vp-p) amplitude to 1V, with no voltage or phase offset.

Vibration amplitude will be adjusted using the “volume” knob on the audio amplifier as opposed to changing the input voltage on the signal generator. Most audio equipment’s maximum input voltage is 1V p-p with no voltage offset, so do not adjust these settings.

Some signal generators are more programable or have more functionalities than others. There is not enough information sent from the MRI scanner to the signal generator inherently to cause any of these changes, but changes in frequency and/or cycles after a certain amount of time or cycles can be programed into some signal generators. For the signal generator in the photos, this option does not exist, and we would need to change frequencies and cycles manually.

Alternatively, a microcontroller could be used as an intermediary between the trigger sent from the scanner and the signal generator to augment the signal generator’s capabilities. Therefore, the signal generator could then be set either manually from a remote location (i.e., the MRI control room), or automatically based on the output from the scanner should the sequence output a different trigger signal dependent on the frequency specified. For this case, the sequence can be programmed such that multiple or specific triggering signal trains are sent dependent on the frequency used in the sequence, and the signal generator or microcontroller can be programmed to output the corresponding frequency.

a. To test the vibration output and select the appropriate amplitude, output from the signal generator without external triggering and adjust the volume (use the knob) on the audio amplifier to adjust the amplitude. Leave the knob at the desired amplitude and turn off the signal generator's output.

12. Set up the external triggering and cycle output on the signal generator. Use the 'burst' option on the signal generator to select external triggering as the source for an N-cycles output. Select the appropriate number of cycles. Once again, turn on the output of the signal generator, therefore, the vibration should only begin when triggered by the MRI sequence.

    The number of cycles is dependent on the repetition time (TR) selected and vibration frequency, or rather, TR must be adjusted to the integer number of cycles (n) multiplied by the vibration period (1/f) such that the burst of vibration stops at the end of the TR and begins again at the beginning of the next TR. Therefore, if the TR is set, multiply the TR by the frequency to calculate the integer number of cycles needed for that acquisition. Because there is a minimum TR necessary to require one slice, there is a minimum n to be used as the number of cycles selected on the signal generator. See Figure 8 for the representation of the TR and frequency shown on the MRE sequence diagram.

13. Place the end-effector in the appropriate positioning for the tissue or phantom and begin the MRE scan protocol.

    a. **For MRE of the human brain**, place the end-effector under the head as if it were a pillow. The end-effector will remain in place due to the weight of the head.

    b. **For MRE of a phantom**, place the end-effector on the surface of the phantom and use an MRI-safe strap adhesive bandage to attach the end-effector to the phantom so it does not move from the intended position during MRE.

    c. **For MRE of a human tissue**, place the end-effector on the tissue of interest and use an MRI-safe adhesive bandage to attach the end-effector to the intended location such that it is firmly pressed against the tissue, but not causing pain or discomfort to the patient.

14. For the first proof-of-concept scan of the subject of interest, multiple vibration amplitudes should be tested in order to select the appropriate amplitude for both patient comfort and usefulness in post-processing (Figure 9).

    If the vibration amplitude is too low, shear waves are not generated sufficiently for viscoelastic inversion analysis and results in a low signal-to-noise ratio. If the vibration amplitude is too high, it will both not be comfortable for the patient (in human scans) and will cause excessive shear wave reflection resulting in an inaccurate wavelength-

based stiffness estimate and low octahedral shear strain signal-to-noise ratio(McGarry et al., 2011) in areas surrounding internal boundaries.

Prior to the proof-of-concept scan, the vibration amplitude and frequency response of the weighted and/or unweighted end-effector can be measured using laser doppler vibrometry to determine suitability. After the proof-of-concept scans, wavefield images and octahedral shear strain signal-to-noise ratio (OSS-SNR) to quantitatively observe vibration quality in the tissue. The OSS-SNR should be relatively uniform within the tissue volume, and asymmetry is likely indicative of a scanning artifact, lack of vibration amplitude in one part of the tissue, or internal wave reflection due to too high of a vibration amplitude. Alternatively, a lack of amplitude in one part of the tissue will be concurrent with a lack of amplitude in the wavefield image. More details regarding quantitative troubleshooting notes can be found in the “Understanding Results” section.

At the end of Basic Protocol 1, the follow should have been achieved: (1) Active components (subwoofer, amplifier, signal generator) have been selected based on the intended use; (2) The subwoofer has been modified and an end-effector shape has been chosen and manufactured; (3, optional) The vibration amplitude and frequency response of the end effector has been verified using a laser doppler vibrometer or other similar system; (4) The entire setup has been implemented in the MRI equipment and scanner rooms; and (5) A proof of concept scan has been performed on phantom or human, and wavefield images and OSS-SNR has been calculated for this scan to evaluate the vibration within the phantom or tissue.

BASIC PROTOCOL 2:

Design, Construction, and Implementation of a Piezoelectric MRE Actuator for Localized Excitation in Phantom Models

The objective of Basic Protocol 2 is to design, construct, and implement a piezoelectric MRE actuator for phantom research purposes using all commercially available components. While the actuator designed in Basic Protocol 1 can be used on a phantom to apply distributed harmonic deformation across the entire surface, this actuator design is for phantom MRE only, and specifically for applying localized harmonic deformation. Additionally, some phantom materials are not conducive for surface harmonic deformation due to either size or surface texture. Localized deformation as opposed to distributed deformation is preferred when investigating wave propagation in all three directions as opposed to determining material stiffness, and for investigations involving multiple material types and/or boundaries.

Materials: A full description of each component as it appears in our configuration is listed next to the general component name in italics. These components can be replaced with those that perform the same function, as described in the protocol.

Active Actuation Components: MRI-compatible Piezoelectric Actuator*: Cedrat Technologies APA150NM*

Linear Amplifier for Piezo: *Cedrat Technologies LA75C*

Signal generator: *RIGOL DG1022 Series Dual-Channel Function/Arbitrary Waveform Generator*

Appropriate cabling for active components*: two Monoprice 75-ohm BNC Male connector BNC Cables- 10 Feet*

Passive Holder/Attachment Components: Anycubic i3 Mega 3-D Printer (or similar machine)

Polylactic Acid (PLA) 3-D Printer Filament: *eSUN PLA PRO (PLA+) 3D Printer Filament, 1kg Spool, 1.75mm, Gray*

MRI-compatible phantom holder material and double sided tape (Dependent on desired design)

Phantom Material (silicone, agar, or other material)

Philips-Head screwdriver (dependent on piezoelectric actuator selected)

CNC machine, laser cutter, or jigsaw and power drill

Phantom Holder Example Design (Square, to fit in 16-channel Siemens Healthineers headcoil): 0.5” thick clear acrylic sheet: *McMaster-Carr: 24” × 24” 1/2” Thick clear cast acrylic sheet (Catalog Number 8560K268)*

1/8” thick clear acrylic sheet: *McMaster-Carr: 12” × 12” 1/8” Thick clear cast acrylic sheet (Catalog Number 8560K239)*

Double sided tape: *Amazon: Double Sided Tape Heavy Duty-1/2” 10’ Acrylic Strong Adhesive Removable Double Sided Mounting Tape Clear*

Nylon Screws: *McMaster-Carr: Metric Nylon Pan Head Phillips Screws, 3M, 12mm length (Catalog Number 92492A719)*

Soft foam

Hot glue gun and hot glue or calking silicone

Protocol Steps with *Step Annotations:*

Component Selection:

1. Select an MRI-safe/compatible piezoelectric actuator and corresponding linear amplifier (CEDRAT actuator and amplifier are shown in Figure 11). The frequency response of the actuator and amplifier should be in the appropriate

range for intended use, generally 30–200Hz. The manufacturer of the piezoelectric actuator should recommend a compatible linear amplifier.

2. Select a signal generator capable of being triggered by an external TTL signal to output a specified signal burst.

3. Select the appropriate cabling to connect the input of the piezoelectric actuator to the output of the amplifier, the input of the amplifier to the output of the signal generator, and the external triggering input of the signal generator to the TTL trigger output of the MRI scanner. Ensure that the cable connecting the piezoelectric actuator to the amplifier is long enough to reach from the MRI equipment room, through the waveguide, and into the MRI scanner bore.

   The appropriate cabling to connect the piezoelectric actuator to the amplifier should be included with the purchase of the device. A BNC male-BNC male cable was used in our case to connect the input of the amplifier to the output of the signal generator. In our case, the TTL output of the MRI scanner and TTL triggering input of the signal generator requires a BNC male-BNC male cable, although this is dependent on the MRI scanner setup.

4. Select MRI-compatible materials and construct a non-metallic phantom holder to both contain the phantom, as well as hold the piezoelectric actuator in the intended position, ensuring that it fits inside of the MRI coil that is going to be used for the MRI scanning experiments. *An example of a design is shown in* Figure 12, *however, any phantom shape required can be manufactured.*

Building and Manufacturing

5. Manufacture and build the phantom holder designed in the previous step.

   a. Use a CNC machine, laser cutter, jigsaw, or other equivalent machine to cut one 15.2 cm × 15.2cm piece, four 10.16 cm × 13.97cm pieces, one 11.18 cm × 5.08cm piece, one 5.08 cm × 5.08cm piece, and one 5.08cm × 3.17cm piece from the 0.5” thick acrylic sheet. In the center of the face of the 15.2 cm × 15.2cm piece, cut a 0.25cm deep, 0.35cm wide slit in a 9.5 cm × 9.5cm square.

   b. Use a CNC machine, laser cutter, jigsaw, or other equivalent machine to cut four 10.41 cm × 9.84cm pieces from the 1/8” thick acrylic sheet.

   c. Place the four 1/8” thick pieces in the 9.5 cm × 9.5cm square slit that was cut in the face of the 15.2 cm × 15.2cm piece and secure with hot glue or calking silicone, ensuring that there are no air holes in the seams by pouring water into the completed box and checking for leaks. This is the cavity in which the phantom will cure (purple in Figure 12).

   d. Line up the four 10.16×13.97cm pieces on the outer edges of the 15.2×15.2cm piece and secure with double sided tape. These are the outer walls of the holder (orange in Figure 12).

e. Drill a 0.25cm diameter hole through the 11.18cm × 5.08cm piece, in the center of the 5.08cm width, and 1.25cm away from the end in the 11.18cm dimension. Drill a 0.6cm deep, 0.6cm diameter countersink on one side of the piece. On the other side, centered on the 0.25cm hole, cut a 0.5 cm × 0.9cm rectangular countersink.

f. Attach the 11.18 cm × 5.08cm piece, 5.08 cm × 5.08cm piece, and 5.08cm × 3.17cm piece together and to the outer wall using double stick tape as shown in Figure 12, with the 0.25cm diameter hole facing the center of the phantom holder, and the rectangular countersink facing down, towards the base.

g. Place the foam in between the inner and outer walls. These are intended to dampen any vibration.

6. Using a CAD software, design and subsequently 3-D print (using PLA+ lament) a vibration end-effector to be submerged into the phantom on one end and connected (via nylon screw) to the piezoelectric actuator on the other side.

   An example design of an end effector in place is shown in Figure 12.

7. Attach the piezoelectric actuator to the phantom holder, and the end effector to the piezoelectric actuator such that the end effector is extending into the area in which the phantom material will be poured (Figure 12(a)).

   Screw (using the nylon screws) one side of the piezoelectric actuator to the end effector, and the other side of the actuator to the 11.18cm × 5.08cm piece using the 0.25cm diameter hole and countersinks to fully secure it into position.

8. Mix the phantom material as desired and pour the liquid phantom material into the phantom holder such that the end effector is partially submerged and allow the phantom to cure around the end effector (Figure 12(b)).

   Good coupling between the end effector and the phantom material is required for shear wave transmission, so it is important for the end effector to be submerged in the phantom material and for the phantom to cure around the end effector as opposed to inserting the end effector into, or pressing it onto, the cured phantom’s surface.

Implementation and Testing

9. Once the phantom has fully cured, place the phantom holder with the piezoelectric actuator attached into the MRI coil, and run the actuator cable away from the phantom and through the waveguide into the MRI equipment room.

10. Place the amplifier for the piezoelectric actuator and the signal generator into the MRI equipment room. Attach the cables from the piezoelectric actuator to the appropriate output on the amplifier and attach the input of the amplifier to the output of the signal generator. Subsequently, use the appropriate cabling to

connect the TTL trigger output of the scanner to the 'TTL external triggering' port on the signal generator.

11. Turn on the signal generator and set the frequency to the desired vibration frequency and the Vp-p amplitude to 5V, with a 2.5 voltage-DC offset and no phase offset. *These voltage values and operation of the amplifier/actuator setup should be based on the information provided in the data sheet for the selected components*

12. Set up the external triggering and cycle output on the signal generator. Use the 'burst' option on the signal generator to select external triggering as the source for an N-cycles output. Select the appropriate number of cycles. Once again, turn on the output of the signal generator, therefore, the vibration should only begin when triggered by the MRI sequence (Figure 13(a,b)).

The number of cycles is dependent on the TR selected and vibration frequency. Multiply the TR by the frequency to calculate the integer number of cycles needed for that acquisition. See Figure 8 for the representation of the TR and frequency shown on the MRE sequence diagram.

a. To test the vibration output and select the appropriate amplitude, output from the signal generator without external triggering.

Prior to the proof-of-concept scan, the stroke length and frequency response of the weighted and/or unweighted piezoelectric actuator can be measured using laser doppler vibrometry to determine suitability. After the proof-of-concept scans, wavefield images and octahedral shear strain signal-to-noise ratio (OSS-SNR) to quantitatively observe vibration quality in the phantom material. The OSS-SNR should be uniform within the phantom, and asymmetry is likely indicative of a scanning artifact, lack of vibration amplitude in one part of the phantom, or internal wave reflection due to too high of a vibration amplitude. Alternatively, a lack of amplitude in one part of the phantom will be concurrent with a lack of amplitude in the wavefield image. More details regarding quantitative troubleshooting notes can be found in the "Understanding Results" section.

At the end of Basic Protocol 2, the follow should have been achieved: (1) Active components (piezoelectric actuator, amplifier, signal generator) have been selected based on the intended use; (2) An end-effector shape has been chosen and manufactured, and the phantom holder has been designed and manufactured; (3, optional) The vibration amplitude and frequency response of the piezoelectric actuator has been verified using a laser doppler vibrometer or other similar system; (4) The entire setup has been implemented in the MRI equipment and scanner rooms, and a phantom material has been chosen; and (5) A proof of

concept scan has been performed on the phantom, and wavefield images and OSS-SNR has been calculated for this scan to evaluate the vibration within the phantom.

COMMENTARY:

Background Information:

Magnetic resonance elastography (MRE) is a technique for determining the mechanical response of soft materials using applied harmonic deformation of the material and a motion sensitive magnetic resonance imaging (MRI) sequence. Use of this technique on human tissue (e.g., liver, brain) can elucidate significant information about its health and development. The applied harmonic deformation used in MRE is generated by an actuator, transmitted in bursts of a specified duration, and synchronized with the MR signal excitation. Because this harmonic vibration must be induced in the tissue in synchronization with the motion encoding gradient (MEG) (Hirsch et al., 2017; Muthupillai et al., 1996), this process requires a type of harmonic actuator that can be used to actuate tissue inside the MRI machine. Therefore, this actuator must be MR compatible, or at least the part of the driver unit that is used inside the scanner room should be MR compatible. The actuator must also be able to provide a wide range of vibration amplitudes and frequencies, as different tissue types require different parameters, generally 45–80Hz for the heart, 40–70Hz for the kidney or liver, 30–150Hz for skeletal muscle, 40–60 for the pancreas, 65–300Hz for the breast, or 25–100Hz for the brain(Arani, Glaser, et al., 2017; Asbach et al., 2010; Barnhill et al., 2013, 2017; Bensamoun et al., 2006; Dittmann et al., 2017; Etchell et al., 2017; Feng et al., 2018; Guo et al., 2013; Hamhaber et al., 2010; Hawley et al., 2017; Hiscox et al., 2020; Hollis et al., 2016; Johnson et al., 2016; Kennedy et al., 2020; Kurt et al., 2019; Lee et al., 2012; Marticorena Garcia et al., 2018; Morisaka et al., 2017; Papazoglou et al., 2006; Plewes et al., 2000; Rump et al., 2007; Sack et al., 2002, 2013; Shi et al., 2015, 2018; Mikio Suga et al., 2001; Van Houten et al., 2003; Wassenaar et al., 2016; Xu et al., 2007; Zhang et al., 2011). The frequency range (bandwidth) of the MRE actuator should match the frequency range necessary for the tissue of interest. Additionally, because biological tissues exhibit viscoelastic behavior, the mechanical response of tissue is dependent on loading speed, or in the case of MRE, the frequency of actuation. Therefore, some studies use multifrequency MRE, in which the vibration is applied and encoded at different frequencies to determine the viscoelasticity(Kurt et al., 2019; Lipp et al., 2013; Neumann, Lehnart, et al., 2018; E Ozkaya et al., 2021).

There are three main categories of MRE actuator. First, there are indirect actuators (usually pneumatic) that use an active driver outside of the scanner room and a passive driver inside the scanner(Asbach et al., 2008; Chang et al., 2016; Chaze et al., 2019; Feng et al., 2018; Freimann et al., 2012; Gruwel et al., 2010; Latta et al., 2011; *MR Elastography | Resoundant Inc.*, n.d.; Meng Yin et al., 2008). Second, an electromagnetic coil/coil(s) can be used to induce vibration by using the static magnetic field by using current to induce rotary motion according to Lorentz Law(Uffmann et al., 2001). This rotary motion is then transferred to the tissue using some type of vibration pad or bite-bar (for brain MRE)(Hamhaber et al., 2003, 2010; Liu et al., 2009; Sack et al., 2002; M. Suga et al., 2003; Uffmann et al., 2001). Third, the actuator can apply the vibration directly to the tissue of interest, where a fully MR

compatible, small actuation unit, usually driven by air pressureor piezoelectric crystals, are attached to the tissue of interest(Brauck et al., 2007; Gordon-Wylie et al., 2018; Namani et al., 2009; Neumann, Bichert, et al., 2018; Numano et al., 2013; Rossman et al., 2003; Runge et al., 2019; Uffmann et al., 2002; Z. Yin et al., 2017). Each of these actuator types has their own sets of benefits and drawbacks. There is currently a need for research specific MRE actuators for various tissue types at multiple field strengths. While there are other device design papers that describe a specific custom pneumatic actuator (e.g., (Feng et al., 2018; Latta et al., 2011)) for research purposes, there are no papers that describe how to design, build, and implement an MRE actuator in general.

Thus, in this paper, we describe how to design and assemble both a pneumatic MRE actuator and a piezoelectric MRE actuator using all commercially available electronic components for research purposes. In Basic Protocol 1, we discuss how to design, construct, and implement a convertible pneumatic MRE actuator for research purposes on multiple tissue types using all commercially available electronic components. This protocol can be utilized to develop an actuator for MRE of the human brain, other human tissue, or phantom. In Basic Protocol 2, we discuss how to design, construct, and implement a piezoelectric MRE actuator for phantom research purposes using all commercially available components. While the actuator designed in Basic Protocol 1 can be used on a phantom to apply distributed harmonic deformation across the entire surface, this actuator design is for phantom MRE only, and specifically for applying localized harmonic deformation.

Critical Parameters:

Actuator Active Component Considerations: The subwoofer and corresponding power amplifier based on the intended use, as the frequency response of the subwoofer and amplifier should be an appropriate range for the human tissue being imaged. Additionally, the subwoofer should have rubber cones as opposed to fabric cones in order to maintain air pressure between the cone and the acrylic sheet. For power considerations, audio equipment typically has an impedance of 2ohms or 4ohms. Most equipment specifications of subwoofers list one or the other, but technical specifications of amplifier will list both, as they can usually amplify at either impedance. The impedance of the subwoofer needs to be considered to ensure that the correct specifications are being considered for the amplifier. Additionally, the maximum power output of the audio amplifier should be greater than the maximum power handling of the subwoofer at the impedance of the subwoofer for obtaining the maximum amplitude the subwoofer is capable of outputting. Generally, the TTL output of the MRI scanner and TTL triggering input of the signal generator requires a BNC male-BNC male cable, but audio cabling is not standardized, so the cabling required is dependent on the selected components. The output of the signal generator should be 1V p-p maximum with no voltage offset, as this is most audio equipment’s maximum allowable input without causing damage to the equipment. Vibration amplitude will the adjusted using the “volume” knob on the audio amplifier as opposed to changing the input voltage on the signal generator.

Piezoelectric Actuator Considerations: The commercial piezoelectric actuator itself and the cabling required to connect the actuator to the amplifier must be MRI-safe. This

may require approval from an MRI safety committee or other administrative approval. The phantom holder must also be able to fit inside of whatever coil is being used during the scans. A 16-channel head coil was used during our scans due to its ability to acquire with high SNR, however this does impose a size restriction. Therefore, the size of the phantom is limited, and the phantom holder must be designed to fit within these specifications. The voltage and voltage offset values, instead of being one set number as it is in audio equipment, are determined by the manufacturer. This is likely in the device's datasheet, although if it is not, this information can be acquired from the manufacturer's technical services or after-sales department. Proper operation (including voltage and frequency settings) is essential for preventing damage to the equipment during use, so it is recommended that the actuator is only driven within the frequency and voltage range that the actuator and cabling is rated for. The frequency range, or bandwidth, of the piezoelectric actuator should therefore match the requirements for the study being performed. Additionally, because of the power in the cabling, it is recommended that the cable is kept as far from the phantom as possible, or artifacts can occur, obscuring part of the captured wavefield image (Figure 13(c)).

General Vibration Considerations: If the vibration amplitude is too low, shear waves are not generated sufficiently for viscoelastic inversion analysis and results in a low signal-to-noise ratio. If the vibration amplitude is too high, it will both not be comfortable for the patient (in human scans) and will cause excessive shear wave reflection resulting in an inaccurate wavelength-based stiffness estimate and low octahedral shear strain signal-to-noise ratio in areas surrounding internal boundaries. After the first set of proof-of-concept scans, both the calculation of wavefield images and octahedral shear signal-to-noise ratio (OSS-SNR) can be used to determine if the vibration amplitude is appropriate. A lack of amplitude in one part of the tissue will be concurrent with a lack of amplitude in the wavefield image, so calculating and observing the wavefield, especially in a uniform phantom, is an important step in determining if the vibration amplitude is at an appropriate level. A secondary method to determine if the vibration amplitude is appropriate and directed in the correct direction is to calculate OSS-SNR. The OSS-SNR should be uniform within the phantom, and asymmetry is likely indicative of a scanning artifact, lack of vibration amplitude in one part of the tissue, or internal wave reflection due to too high of a vibration amplitude. More information on both of these parameters can be found in the "Understanding Results" section. Therefore, multiple amplitudes should be tested prior to determining the final scanning protocol for a particular study. The external triggering of the signal generator should be run on an N-cycles burst setting. The number of cycles per burst to run the signal generator for is dependent on the TR selected and vibration frequency. Multiply the TR by the frequency to calculate the integer number of cycles needed for that acquisition. Finally, the coupling between the end-effector and the tissue or phantom is crucial to vibration transfer. For the pneumatic actuator, the end-effector pillow should be firmly pressed against the surface of the tissue or phantom, either held down by body weight (if under the subject) or held on tightly using MRI-safe adhesive bandage. For the piezoelectric actuator, the phantom should cure around the end effector to ensure full adhesion.

Troubleshooting:

Human Brain End Effector Challenges: Since the specific application we worked on here is the human brain, we implemented multiple iterations of end-effector design based on multiple technology development scans on healthy human volunteers. Multiple pillow designs were manufactured and tested for both effective, even, vibration application and patient comfort, resulting in the final design that matches the shape of the head coil without any sharp ridges, and thin enough to allow us to scan a diverse patient population (Figure 14). The size and shape are dependent on the head coil, and due to challenges with the head coil size at 7T MRI scanners, our pillow design required several iterations, but the same design issues arise for many multi-channel head coils. The initial pillow design did not provide sufficient vibration, while the second pillow design provided enough vibration but was not comfortable to lay on for the duration of the scan. The third pillow design also provided sufficient vibration but was not fully comfortable due to the ridge in the back. This design was also too thick to allow us to scan a diverse patient population. The fourth design initially did not provide sufficient vibration due to the pillow compressing under the weight of the head, however, by adding soft supports to the inside of the pillow where the head rests, the pillow was both comfortable and provided sufficient vibration. Due to concerns about uneven application of vibration, a modification to the inlet to make it central resulted in the final pillow design.

Subwoofer is Not Outputting Sound/Piezoelectric Actuator is not Vibrating (General): The first step for troubleshooting this problem is to ensure that every component is plugged in, powered on, and on the correct settings, and that the signal generator is set to output a consistent signal with no external triggering. The next step is to ensure that all the cable connections are snug and to utilize a multimeter to check that all cables are working properly; if any are loose or not working, replace the cable and attempt to run the device again. If this is not the issue, next, use a multimeter or oscilloscope to ensure that the signal generator is outputting a signal as expected; if not, the signal generator should be replaced with a different one. If that is not the problem, use a multimeter or oscilloscope to ensure that the amplifier is outputting an amplified signal as expected; if not, the amplifier should be sent off for repair or returned and a new one purchased. If none of the previous steps have revealed the issue, the problem is likely the subwoofer (in the case of Basic Protocol 1) or the piezoelectric actuator (in the case of Basic Protocol 2).

Subwoofer is Not Outputting Sound/Piezoelectric Actuator is not Vibrating (During Scans): If the subwoofer is outputting/the piezoelectric actuator is vibrating when the signal generator is set to output a consistent signal with no external triggering, it is first important to check cable connections. The external triggering port in the equipment room should be connected via cable to the MRI scanner. To ensure that a trigger signal is being output, connect the scanner's external triggering port (in the equipment room) to an oscilloscope and run the MRE sequence to observe outputs. If there is no trigger signal output, it may need to be enabled within the sequence, or the cable connections are not correct/a cable has broken; test the cables to see if this is the case. If the trigger signal is being output, ensure that the correct external triggering port is being used on the signal generator; try a new signal generator if this does not solve the problem.

Subwoofer Stops Outputting Sound Above a Certain Volume Level: This problem can occur when the amplifier overvolts, and it is important to immediately turn the amplifier down and off when this occurs to avoid damage to the equipment. If this is consistently occurring at a 1Vp-p input to the amplifier, it is likely because the maximum power output of the audio amplifier is not greater than the maximum power handling of the subwoofer at the impedance of the subwoofer. One option is to simply mark on the amplifier what level on the knob this occurs at and not turn the knob past that mark. Another option is to reduce the input voltage. Finally, the recommended option for obtaining the maximum amplitude the subwoofer is capable of outputting is to replace the power amplifier with a more powerful option.

Excessive Damping from Subwoofer Cone to End Effector: This excessive dampening can occur due to tubing connections, or the softness of the tubing used. If the tubing is too soft, it can directly dampen the air pressure waves, in which case it should be switched out for stiffer tubing. Any tube splitter or connector will also cause dampening, as the air pressure wave will reflect and cause destructive interference; it is recommended that one continuous piece of tubing (with no connectors) connects the subwoofer cone to a single-inlet end effector.

Understanding Results:

It is imperative to determine that the actuator is operating at the correct frequency and with sufficient amplitude before use in the intended tissue. One method for determining this is to use, as an example, a laser doppler vibrometer to both achieve an accurate estimated of the unloaded actuator's frequency and its frequency response(Curtis et al., 2012; E Ozkaya et al., 2021; Triolo et al., 2021). This method can also be used to determine the time delay from signal generator output to end-effector vibration in the case of the pneumatic actuator(Triolo et al., 2021). This time delay can also be calculated based on the speed of sound in the length of tubing, but empirical measurement is far more accurate in this case. Once it is confirmed that the actuator is producing vibration at the expected amplitude and frequency, the next step is to determine if the actuator is coupled with the tissue or phantom well enough to produce shear waves with sufficient SNR in the collected phase images. When looking at a wavefield image in a homogeneous material (a phantom, typically used for validation) the shear wave should be clearly visible with the expected wavelength and propagation speed based on stiffness-based estimates and as shown in Figures 9 and 15. Should the wavefield look over-saturated (where the phase is wrapped multiple times for one wave peak), the vibration amplitude should be decreased, and should the expected wavelength be barely visible, the amplitude increased. However, this is difficult to determine in human tissue, for example the brain shown in Figure 9.

One way to determine if the vibration amplitude is appropriate and directed in the correct direction is to perform a calculation of octahedral shear strain signal-to-noise ratio (OSS-SNR)(McGarry et al., 2011). The OSS-SNR should be uniform within the tissue of interest, and any asymmetry is likely indicative of a scanning artifact, lack of vibration amplitude in one part of the tissue, or internal wave reflection. Generally, an average OSS-SNR of 3 or above is considered acceptable(McGarry et al., 2011). This will also be reflected

in the stiffness reconstruction of the tissue or phantom. A lack of amplitude in one part of the tissue will be concurrent with a lack of amplitude in the wavefield image. To fix this asymmetry due to lack of amplitude in one part of the tissue, the actuator end-effector should be repositioned, or the amplitude increased to increase the penetration of the traveling wave. Internal wave reflection, usually due to boundaries and/or shear wave interactions, can be caused by the application of an amplitude that is too high. Not only will this cause asymmetry in OSS-SNR and stiffness reconstruction maps, there will also be visible oversaturation in the wavefield images. In this case, the amplitude should be decreased.

Overall, the purpose of MRE is to determine the mechanical properties of tissues or other materials. Performing MRE on a tissue can provide information on different structures within that tissue based on their mechanical properties (*i.e.*, magnitude of the complex shear modulus, damping ratio) using a viscoelastic inversion (*e.g.*, Local frequency estimation, algebraic inversion, or nonlinear inversion) calculation on the capture wavefield images (Honarvar et al., 2017; Maharjan et al., 2020; Van Houten et al., 2001). In the brain specifically (as this is our application), these properties can provide information on cell density, myelination, inflammation, and functional activation(Fehlner et al., 2014; Guo et al., 2013; Hiscox et al., 2018, 2020; Huston et al., 2015, 2016; Johnson et al., 2016; Kurt et al., 2019; McIlvain et al., 2018; Murphy et al., 2016; Pattison et al., 2009; Perry et al., 2017; Sack et al., 2009, 2011; Streitberger et al., 2011; Zhang et al., 2011). These mechanical parameters (*i.e.*, magnitude of the complex shear modulus, damping ratio) can then be used to diagnose pathologies such as multiple sclerosis (MS), Alzheimer's disease, and Parkinson's disease, or indicate disease progress(ElSheikh et al., 2017; Gerischer et al., 2016; Hiscox et al., 2019; Johnson et al., 2017; Lipp et al., 2013, 2018; Murphy et al., 2011, 2016; Streitberger et al., 2012; Wuerfel et al., 2010). As stated earlier, MRE is used by pathologists to diagnose liver fibrosis, and other diagnostic applications of MRE, such as breast cancer, prostate cancer, and pancreatic masses, have been suggested and investigated (Arani, Eskandari, et al., 2017; Doyley et al., 2003; Glaser et al., 2006; *MR Elastography | Resoundant Inc.*, n.d.; Shah et al., 2004; Shi et al., 2018).

Time Considerations:

The lead times on components can range from only 1 day for smaller materials to several weeks for the complex electronic components such as the piezoelectric actuator and amplifier, audio amplifier, subwoofer, and signal generator. These major components should be ordered well in advance of the planned experiments, as smaller components that correspond to a specific major component will likely need to be ordered after these major components arrive (e.g., matching cabling, screws of a specific size).

Manufacturing the end-effector via 3-D printing, gluing, clamping, etc. will take between 3 hours (for the piezoelectric end effector) and 1 day (pneumatic human brain end effector).

Cost Considerations: For the pneumatic actuator, the most costly components are the signal generator, audio amplifier, and subwoofer. Used/refurbished signal generators with the required functionality range from about $150 to $400, while purchasing new can cost

upwards of $1000. The cost of audio amplifier will range widely based on power, with low wattage amplifiers costing under $100 and high wattage costing over $500. The 3000W dual-channel amplifier shown in Figure 2 costs around $300. From the same brand, an amplifier twice as powerful costs around $500. The subwoofer cost ranges based on size and quality, generally from $50–250, but the subwoofer shown in Figure 2 costs about $170. The cost of 3D printing, machining, and assembly is dependent on the materials, personnel, and equipment available. For the piezoelectric actuator, the cost of the actuator itself was around $2000 and the cost of the used/refurbished amplifier was $400. A new amplifier would cost in the $1000–2000 range. The same signal generator as mentioned for the pneumatic actuator was used here. Various phantom materials of varying costs can be used with this protocol, but the least costly would be Knox unflavored gelatin at around $15 per pound. Again, the cost of 3D printing, machining, and assembly is dependent on the materials, personnel, and equipment available.

ACKNOWLEDGEMENTS:

We would like to acknowledge funding from NSF awards 1953323 and 1826270.

DATA AVAILABILITY STATEMENT:

All final CAD models referenced in this article will be made available for download.

LITERATURE CITED:

Arani A, Eskandari A, Ouyang P, & Chopra R (2017). A novel high amplitude piezoceramic actuator for applications in magnetic resonance elastography: a compliant mechanical amplifier approach. Smart Materials and Structures, 26(8), 1–10. 10.1088/1361-665x/aa71f2

Arani A, Glaser KL, Arunachalam SP, Rossman PJ, Lake DS, Trzasko JD, Manduca A, McGee KP, Ehman RL, & Araoz PA (2017). In vivo, high-frequency three-dimensional cardiac MR elastography: Feasibility in normal volunteers. Magnetic Resonance in Medicine, 77(1), 351–360. 10.1002/mrm.26101 [PubMed: 26778442]

Asbach P, Klatt D, Hamhaber U, Braun J, Somasundaram R, Hamm B, & Sack I (2008). Assessment of liver viscoelasticity using multifrequency MR elastography. Magnetic Resonance in Medicine, 60(2), 373–379. 10.1002/mrm.21636 [PubMed: 18666132]

Asbach P, Klatt D, Schlosser B, Biermer M, Muche M, Rieger A, Loddenkemper C, Somasundaram R, Berg T, Hamm B, Braun J, & Sack I (2010). Viscoelasticity-based staging of hepatic fibrosis with multifrequency MR elastography. Radiology, 257(1), 80–86. 10.1148/radiol.10092489 [PubMed: 20679447]

Badachhape AA, Okamoto RJ, Johnson CL, & Bayly PV (2018). Relationships between scalp, brain, and skull motion estimated using magnetic resonance elastography. Journal of Biomechanics, 73, 40–49. 10.1016/j.jbiomech.2018.03.028 [PubMed: 29580689]

Barnhill E, Hollis L, Sack I, Braun J, Hoskins PR, Pankaj P, Brown C, van Beek EJR, & Roberts N (2017). Nonlinear multiscale regularisation in MR elastography: Towards fine feature mapping. Medical Image Analysis, 35, 133–145. 10.1016/j.media.2016.05.012 [PubMed: 27376240]

Barnhill E, Kennedy P, Hammer S, Van Beek EJR, Brown C, & Roberts N (2013). Statistical mapping of the effect of knee extension on thigh muscle viscoelastic properties using magnetic resonance elastography. Physiological Measurement, 34(12), 1675–1698. 10.1088/0967-3334/34/12/1675 [PubMed: 24254405]

Bensamoun SF, Ringleb SI, Littrell L, Chen Q, Brennan M, Ehman RL, & An KN (2006). Determination of thigh muscle stiffness using magnetic resonance elastography. Journal of Magnetic Resonance Imaging, 23(2), 242–247. 10.1002/jmri.20487 [PubMed: 16374878]

Brauck K, Galbán CJ, Maderwald S, Herrmann BL, & Ladd ME (2007). Changes in calf muscle elasticity in hypogonadal males before and after testosterone substitution as monitored by magnetic resonance elastography. European Journal of Endocrinology, 156(6), 673–678. 10.1530/EJE-06-0694 [PubMed: 17535867]

Chang W, Lee JM, Yoon JH, Han JK, Choi BI, Yoon JH, Lee KB, Lee KW, Yi NJ, & Suh KS (2016). Liver fibrosis staging with MR elastography: Comparison of diagnostic performance between patients with chronic hepatitis B and those with other etiologic causes. Radiology, 280(1), 88–97. 10.1148/radiol.2016150397 [PubMed: 26844364]

Chaze CA, McIlvain G, Smith DR, Villermaux GM, Delgorio PL, Wright HG, Rogers KJ, Miller F, Crenshaw JR, & Johnson CL (2019). Altered brain tissue viscoelasticity in pediatric cerebral palsy measured by magnetic resonance elastography. NeuroImage: Clinical, 22. 10.1016/j.nicl.2019.101750

Curtis ET, Zhang S, Khalilzad-Sharghi V, Boulet T, & Othman SF (2012). Magnetic resonance elastography methodology for the evaluation of tissue engineered construct growth. Journal of Visualized Experiments, 60, 1–6. 10.3791/3618

Dittmann F, Tzschätzsch H, Hirsch S, Barnhill E, Braun J, Sack I, & Guo J (2017). Tomoelastography of the abdomen: Tissue mechanical properties of the liver, spleen, kidney, and pancreas from single MR elastography scans at different hydration states. Magnetic Resonance in Medicine, 78(3), 976–983. 10.1002/mrm.26484 [PubMed: 27699875]

Doyley MM, Weaver JB, Van Houten EEW, Kennedy FE, & Paulsen KD (2003). Thresholds for detecting and characterizing focal lesions using steady-state MR elastography. Medical Physics, 30(4), 495–504. 10.1118/1.1556607 [PubMed: 12722801]

ElSheikh MM, Arani A, Perry A, Boeve BF, Meyer FB, Savica R, Ehman RL, & Huston J (2017). MR elastography demonstrates unique regional brain stiffness patterns in dementias. AJR Am J Roentgenol, 209(2), 403–408. 10.2214/AJR.16.17455.MR [PubMed: 28570101]

Etchell E, Jugé L, Hatt A, Sinkus R, & Bilston LE (2017). Liver stiffness values are lower in pediatric subjects than in adults and increase with age: A multifrequency MR elastography study. Radiology, 283(1), 222–230. 10.1148/radiol.2016160252 [PubMed: 27755913]

Fehlner A, Guo J, Streitberger KJ, Hirsch S, Braun J, & Sack I (2014). The viscoelastic response of the human brain to functional activation detected by magnetic resonance elastography. Proceedings of the 22nd Annul Meeting of ISMRM, Milan.

Feng Y, Zhu M, Qiu S, Shen P, Ma S, Zhao X, Hu C. hong, & Guo L (2018). A multi-purpose electromagnetic actuator for magnetic resonance elastography. Magnetic Resonance Imaging, 51, 29–34. 10.1016/j.mri.2018.04.008 [PubMed: 29679635]

Freimann FB, Streitberger KJ, Klatt D, Lin K, McLaughlin J, Braun J, Sprung C, & Sack I (2012). Alteration of brain viscoelasticity after shunt treatment in normal pressure hydrocephalus. Neuroradiology, 54(3), 189–196. 10.1007/s00234-011-0871-1 [PubMed: 21538046]

Gerischer LM, Fehlner A, Köbe T, Braun J, Sack I, & Agnes F (2016). High resolution MR elastography of the hippocampus as a novel biomarker for Alzheimer's disease? Clinical Neurophysiology, 127(FV 12), e216–e217. 10.1016/j.clinph.2016.05.029

Glaser KJ, Felmlee JP, & Ehman RL (2006). Rapid MR elastography using selective excitations. Magnetic Resonance in Medicine, 55(6), 1381–1389. 10.1002/mrm.20913 [PubMed: 16683257]

Gordon-Wylie SW, Solamen LM, McGarry MDJ, Zeng W, VanHouten E, Gilbert G, Weaver JB, & Paulsen KD (2018). MR elastography at 1 Hz of gelatin phantoms using 3D or 4D acquisition. Journal of Magnetic Resonance, 296, 112–120. 10.1016/j.jmr.2018.08.012 [PubMed: 30241018]

Greenleaf JF, Muthupillai R, Rossman PJ, Lomas DJ, Riederer SJ, & Ehman RL (2000). Measurement of Tissue Elasticity Using Magnetic Resonance Elastography. Review of Progress in Quantitative Nondestructive Evaluation, 16, 19–26.

Greenleaf JF, Muthupillai R, Rossman PJ, Smith J, Manduca A, & Ehman RL (1996). Direct Visualization of Strain Waves by Magnetic Resonance Elastography (MRE). IEEE Ultrasonics Symposium, 467–472.

Gruwel MLH, Latta P, Matwiy B, & Tomanek B (2010). Characterization of food stuffs using Magnetic Resonance Elastography. Food Research International, 43(8), 2087–2092. 10.1016/j.foodres.2010.07.015

Guo J, Hirsch S, Fehlner A, Papazoglou S, Scheel M, Braun J, & Sack I (2013). Towards an Elastographic Atlas of Brain Anatomy. PLoS ONE, 8(8). 10.1371/journal.pone.0071807

Hamhaber U, Grieshaber FA, Nagel JH, & Klose U (2003). Comparison of quantitative shear wave MR-elastography with mechanical compression tests. Magnetic Resonance in Medicine, 49(1), 71–77. 10.1002/mrm.10343 [PubMed: 12509821]

Hamhaber U, Klatt D, Papazoglou S, Hollmann M, Stadler J, Sack I, Bernarding J, & Braun J (2010). In vivo magnetic resonance elastography of human brain at 7 T and 1.5 T. Journal of Magnetic Resonance Imaging, 32(3), 577–583. 10.1002/jmri.22294 [PubMed: 20815054]

Hawley JR, Kalra P, Mo X, Raterman B, Yee LD, & Kolipaka A (2017). Quantification of breast stiffness using MR elastography at 3 Tesla with a soft sternal driver: A reproducibility study. Journal of Magnetic Resonance Imaging, 45(5), 1379–1384. 10.1002/jmri.25511 [PubMed: 27779802]

Hirsch S, Braun J, & Sack I (2017). Magnetic Resonance Elastography: Physical Background and Medical Applications. In Wiley. 10.1038/nm0596-601

Hiscox LV, Johnson CL, McGarry MDJ, Perrins M, Littlejohn A, van Beek EJR, Roberts N, & Starr JM (2018). High-reolution magnetic resonance elastogrohy reveals differences in subcortical gray matter viscoelasticity between young and healthy older adults. Neurobiology of Aging, 65, 158–167. [PubMed: 29494862]

Hiscox LV, McGarry MDJ, Schwarb H, Van Houten EEW, Pohlig RT, Roberts N, Huesmann GR, Burzynska AZ, Sutton BP, Hillman CH, Kramer AF, Cohen NJ, Barbey AK, Paulsen KD, & Johnson CL (2020). Standard-space atlas of the viscoelastic properties of the human brain. Human Brain Mapping, 41(18), 5282–5300. 10.1002/hbm.25192 [PubMed: 32931076]

Hiscox LV, Johnson CL, McGarry MDJ, Marshall H, Ritchie CW, van Beek EJR, Roberts N, & Starr JM (2019). Mechanical property alterations across the cerebral cortex due to Alzheimer's disease. Brain Communications, 2(1). 10.1093/braincomms/fcz049

Hollis L, Barnhill E, Conlisk N, Thomas-Seale LEJ, Roberts N, Pankaj P, & Hoskins PR (2016). Finite element analysis to compare the accuracy of the direct and MDEV inversion algorithms in MR elastography. IAENG International Journal of Computer Science, 43(2), 137–146.

Honarvar M, Sahebjavaher RS, Rohling R, & Salcudean SE (2017). A Comparison of Finite Element-Based Inversion Algorithms, Local Frequency Estimation, and Direct Inversion Approach Used in MRE. IEEE Transactions on Medical Imaging, 36(8), 1686–1698. 10.1109/TMI.2017.2686388 [PubMed: 28333623]

Huston J, Murphy MC, Boeve BF, Fattahi N, Arani A, Glaser KJ, Manduca A, Jones DT, & Ehman RL (2016). Magnetic resonance elastography of frontotemporal dementia. Journal of Magnetic Resonance Imaging, 43(2), 474–478. 10.1002/jmri.24977 [PubMed: 26130216]

Huston J, Perry A, Fattahi N, Arani A, Meyer F, & Ehman R (2015). Magnetic resonance elastography demonstrates increased brain stiffness in normal pressure hydrocephalus. Fluids and Barriers of the CNS, 12(Suppl 1), O38. 10.1007/978-1-4939-1575-0

Johnson CL, Matijevich ES, Cullum ED, McGarry MD, Paulsen KD, Sutton BP, Wszalek TM, & Olivero WC (2016). MR elastography of intercranial tumors: initial experience with high-resolution imaging and nonlinear inversion. ISMRM 2016. 10.1007/s00062-014-0311-9

Johnson CL, Thompson CA, Sandro BM, Edwards TA, Hubbard EA, Klaren RE, Schwarb H, Sutton BP, Pilutti LA, & Motl RW (2017). Multiple sclerosis lesions are softer than surrounding white matter : An MR elastography study. ISMRM 2017 Conference Proceedings.

Kennedy P, Barnhill E, Gray C, Brown C, van Beek EJR, Roberts N, & Greig CA (2020). Magnetic resonance elastography (MRE) shows significant reduction of thigh muscle stiffness in healthy older adults. GeroScience, 42(1), 311–321. 10.1007/s11357-019-00147-2 [PubMed: 31865527]

Kurt M, Wu L, Laksari K, Ozkaya E, Suar ZM, Lv H, Epperson K, Epperson K, Sawyer AM, Camarillo D, Pauly KB, & Wintermark M (2019). Optimization of a Multifrequency Magnetic Resonance Elastography Protocol for the Human Brain. Journal of Neuroimaging, 29(4), 440–446. 10.1111/jon.12619 [PubMed: 31056818]

Kwon OI, Park C, Nam HS, Woo EJ, Seo JK, Glaser KJ, Manduca A, & Ehman RL (2009). Shear modulus decomposition algorithm in magnetic resonance elastography. IEEE Transactions on Medical Imaging, 28(10), 1526–1533. 10.1109/TMI.2009.2019823 [PubMed: 19783495]

Latta P, Gruwel MLH, Debergue P, Matwiy B, Sboto-Frankenstein UN, & Tomanek B (2011). Convertible pneumatic actuator for magnetic resonance elastography of the brain. Magnetic Resonance Imaging, 29(1), 147–152. 10.1016/j.mri.2010.07.014 [PubMed: 20833495]

Lee CU, Glockner JF, Glaser KJ, Yin M, Chen J, Kawashima A, Kim B, Kremers WK, Ehman RL, & Gloor JM (2012). MR Elastography in Renal Transplant Patients and Correlation with Renal Allograft Biopsy- A Feasibility Study. Academic Radiology, 19(7), 834–841. 10.1016/j.acra.2012.03.003 [PubMed: 22503893]

Lipp A, Skowronek C, Fehlner A, Streitberger KJ, Braun J, & Sack I (2018). Progressive supranuclear palsy and idiopathic Parkinson's disease are associated with local reduction of in vivo brain viscoelasticity. European Radiology, 28(8), 3347–3354. 10.1007/s00330-017-5269-y [PubMed: 29460073]

Lipp A, Trbojevic R, Paul F, Fehlner A, Hirsch S, Scheel M, Noack C, Braun J, & Sack I (2013). Cerebral magnetic resonance elastography in supranuclear palsy and idiopathic Parkinson's disease. NeuroImage: Clinical, 3, 381–387. 10.1016/j.nicl.2013.09.006 [PubMed: 24273721]

Liu GR, Gao PY, Lin Y, Xue J, Wang XC, Sui B. Bin, Ma L, Xi ZN, Bai Q, & Shen H (2009). Brain magnetic resonance elastography on healthy volunteers: A safety study. Acta Radiologica, 50(4), 423–429. 10.1080/02841850902751681 [PubMed: 19241188]

Maharjan S, Numano T, Habe T, Ito D, Ueki T, Igarashi K, & Maeno T (2020). Directional Filter, Local Frequency Estimate and Algebraic Inversion of Differential Equation of Psoas Major Magnetic Resonance Elastography. Open Journal of Medical Imaging, 10(01), 1–16. 10.4236/ojmi.2020.101001

Manduca A, Oliphant TE, Dresner MA, Lake DS, Greenleaf JF, & Ehman RL (2002). Comparative Evaluation of Inversion Algorithms for Magnetic Resonance Elastography. Proceedings IEEE International Symposium on Biomedical Imaging, 997–1000.

Marticorena Garcia SR, Grossmann M, Lang ST, Tzschätzsch H, Dittmann F, Hamm B, Braun J, Guo J, & Sack I (2018). Tomoelastography of the native kidney: Regional variation and physiological effects on in vivo renal stiffness. Magnetic Resonance in Medicine, 79(4), 2126–2134. 10.1002/mrm.26892 [PubMed: 28856718]

McGarry MDJ, Van Houten EEW, Perrĩez PR, Pattison AJ, Weaver JB, & Paulsen KD (2011). An octahedral shear strain-based measure of SNR for 3D MR elastography. Physics in Medicine and Biology, 56(13). 10.1088/0031-9155/56/13/N02

McIlvain G, Schwarb H, Cohen NJ, Telzer EH, & Johnson CL (2018). Mechanical properties of the in vivo adolescent human brain. Developmental Cognitive Neuroscience, 34, 27–33. 10.1016/j.dcn.2018.06.001 [PubMed: 29906788]

Meinhold W, Ozkaya E, Ueda J, & Kurt M (2019). Tuneable resonance actuators for magnetic resonance elastography. Frontiers in Biomedical Devices, BIOMED - 2019 Design of Medical Devices Conference, DMD 2019, 1–5. 10.1115/DMD2019-3313

Morisaka H, Motosugi U, Glaser KJ, Ichikawa S, Ehman RL, Sano K, Ichikawa T, & Onishi H (2017). Comparison of diagnostic accuracies of two- and three-dimensional MR elastography of the liver. Journal of Magnetic Resonance Imaging, 45(4), 1163–1170. 10.1002/jmri.25425 [PubMed: 27662640]

MR Elastography | Resoundant Inc. (n.d.). https://www.resoundant.com/

Murphy MC, Huston J, Jack CR, Glaser KJ, Manduca A, Felmlee JP, & Ehman RL (2011). Decreased brain stiffness in alzheimer's disease determined by magnetic resonance elastography. Journal of Magnetic Resonance Imaging, 34, 494–498. [PubMed: 21751286]

Murphy MC, Jones DT, Jack CR, Glaser KJ, Senjem ML, Manduca A, Felmlee JP, Carter RE, Ehman RL, & Huston J (2016). Regional brain stiffness changes across the Alzheimer's disease spectrum. NeuroImage: Clinical, 10, 283–290. 10.1016/j.nicl.2015.12.007 [PubMed: 26900568]

Muthupillai R, Rossman PJ, Lomas DJ, Greenleaf JF, Riederer SJ, & Ehman RL (1996). Magnetic resonance imaging of transverse acoustic strain waves. Magnetic Resonance in Medicine, 36(2), 266–274. [PubMed: 8843381]

Namani R, Wood MD, Sakiyama SE, & Bayly PV (2009). Anisotropic mechanical properties of magnetically aligned fibrin gels measured by magnetic resonance elastography. Journal of Biomechanics, 42, 2047–2053. [PubMed: 19656516]

Neumann W, Bichert A, Fleischhauer J, Stern A, Figuli R, Wilhelm M, Schad LR, & Zollner FG (2018). A novel 3D printed mechanical actuator using centrifugal force for magnetic resonance elastography: Initial results in an anthropomorphic prostate phantom. PLoS ONE, 13(10), 1–14. 10.1371/journal.pone.0205442

Neumann W, Lehnart VR, Vetter Y, Bichert A, Schad LR, & Zöllner FG (2018). Coupled actuators with a mechanically synchronized phase during MR elastography: A phantom feasibility study. Concepts in Magnetic Resonance Part B: Magnetic Resonance Engineering, 48(4), 1–9. 10.1002/cmr.b.21403

Numano T, Kawabata Y, Mizuhara K, Washio T, Nitta N, & Homma K (2013). Magnetic resonance elastography using an air ball-actuator. Magnetic Resonance Imaging, 31(6), 939–946. 10.1016/j.mri.2013.02.001 [PubMed: 23602728]

Ozkaya E, Triolo ER, Rezayaraghi F, Abderezaei J, Meinhold W, Hong K, Alipour A, Kennedy P, Fleysher L, Ueda J, Balchandani P, Eriten M, Johnson CL, Yang Y, & Kurt M (2021). Brain-mimicking phantom for biomechanical validation of motion sensitive MR imaging techniques. Journal of the Mechanical Behavior of Biomedical Materials, 122, 104680. 10.1016/j.jmbbm.2021.104680

Ozkaya Efe, Fabris G, Macruz F, Suar ZM, Abderezaei J, Su B, Laksari K, Wu L, Camarillo DB, Pauly KB, Wintermark M, & Kurt M (2021). Viscoelasticity of children and adolescent brains through MR elastography. Journal of the Mechanical Behavior of Biomedical Materials, 115(December 2020), 104229. 10.1016/j.jmbbm.2020.104229

Papazoglou S, Hirsch S, Braun J, & Sack I (2012). Multifrequency inversion in magnetic resonance elastography. Physics in Medicine and Biology, 57(8), 2329–2346. 10.1088/0031-9155/57/8/2329 [PubMed: 22460134]

Papazoglou S, Rump J, Braun J, & Sack I (2006). Shear wave group velocity inversion in MR elastography of human skeletal muscle. Magnetic Resonance in Medicine, 56(3), 489–497. 10.1002/mrm.20993 [PubMed: 16894586]

Pattison AJ, Lollis SS, Perrinez PR, Weaver JB, & Paulsen KD (2009). MR elastography of hydrocephalus. Proceedings of SPIE - The International Society for Optical Engineering, 7262, 72620A0–8. 10.1117/12.811820

Perry A, Graffeo CS, Fattahi N, ElSheikh MM, Cray N, Arani A, Ehman RL, Glaser KJ, Manduca A, Meyer FB, & Huston J (2017). Clinical Correlation of Abnormal Findings on Magnetic Resonance Elastography in Idiopathic Normal Pressure Hydrocephalus. World Neurosurgery, 99, 695–700. 10.1016/j.wneu.2016.12.121 [PubMed: 28063896]

Plewes DB, Bishop J, Samani A, & Sciarretta J (2000). Visualization and quantification of breast cancer biomechanical properties with magnetic resonance elastography. Physics in Medicine and Biology, 45, 1591–1610. [PubMed: 10870713]

Rossman P, Glaser K, Felmlee J, & Ehman R (2003). Piezoelectric Bending Elements for use as Motion Actuators in MR Elastography. In Proc. Intl. Soc. Mag. Reson. Med (Vol. 11, p. 1075). http://www.google.com/url?sa=t&rct=j&q=piezoelectric bending elements for use as motion actuators in mr elastography&source=web&cd=1&ved=0CE0QFjAA&url=http%3A%2F%2Fcds.ismrm.org%2Fismrm-2003%2F1075.pdf&ei=jlPhTryfG8WztwfWm5H5Aw&usg=AFQjCNE04mOmkt_jsOZLO4_

Rump J, Klatt D, Braun J, Warmuth C, & Sack I (2007). Fractional encoding of harmonic motions in MR elastography. Magnetic Resonance in Medicine, 57(2), 388–395. 10.1002/mrm.21152 [PubMed: 17260354]

Runge JH, Hoelzl SH, Sudakova J, Dokumaci AS, Nelissen JL, Guenthner C, Lee J, Troelstra M, Fovargue D, Stoker J, Nederveen AJ, Nordsletten D, & Sinkus R (2019). A novel magnetic resonance elastography transducer concept based on a rotational eccentric mass: Preliminary experiences with the gravitational transducer. Physics in Medicine and Biology, 64(4). 10.1088/1361-6560/aaf9f8

Sack I, Beierbach B, Wuerfel J, Klatt D, Hamhaber U, Papazoglou S, Martus P, & Braun J (2009). The impact of aging and gender on brain viscoelasticity. NeuroImage, 46(3), 652–657. 10.1016/j.neuroimage.2009.02.040 [PubMed: 19281851]

Sack I, Bernarding J, & Braun J (2002). Analysis of wave patterns in MR elastography of skeletal muscle using coupled harmonic oscillator simulations. Magnetic Resonance Imaging, 20(1), 95–104. 10.1016/S0730-725X(02)00474-5 [PubMed: 11973034]

Sack I, Jöhrens K, Würfel J, & Braun J (2013). Structure-sensitive elastography: On the viscoelastic powerlaw behavior of in vivo human tissue in health and disease. Soft Matter, 9(24), 5672–5680. 10.1039/c3sm50552a

Sack I, Streitberger KJ, Krefting D, Paul F, & Braun J (2011). The influence of physiological aging and atrophy on brain viscoelastic properties in humans. PLoS ONE, 6(9). 10.1371/journal.pone.0023451

Shah NS, Kruse SA, Lager DJ, Farell-Baril G, Lieske JC, King BF, & Ehman RL (2004). Evaluation of renal parenchymal disease in a rat model with magnetic resonance elastography. Magnetic Resonance in Medicine, 52(1), 56–64. 10.1002/mrm.20101 [PubMed: 15236367]

Shi Y, Gao F, Li Y, Tao S, Yu B, Liu Z, Liu Y, Glaser KJ, Ehman RL, & Guo Q (2018). Differentiation of benign and malignant solid pancreatic masses using magnetic resonance elastography with spin-echo echo planar imaging and three-dimensional inversion reconstruction: a prospective study. European Radiology, 28(3), 936–945. 10.1007/s00330-017-5062-y [PubMed: 28986646]

Shi Y, Glaser KJ, Venkatesh SK, Ben-Abraham EI, & Ehman RL (2015). Feasibility of using 3D MR elastography to determine pancreatic stiffness in healthy volunteers. Journal of Magnetic Resonance Imaging, 41(2), 369–375. 10.1002/jmri.24572 [PubMed: 24497052]

Streitberger KJ, Sack I, Krefting D, Pfüller C, Braun J, Paul F, & Wuerfel J (2012). Brain viscoelasticity alteration in chronic-progressive multiple sclerosis. PLoS ONE, 7(1). 10.1371/journal.pone.0029888

Streitberger KJ, Wiener E, Hoffmann J, Freimann FB, Klatt D, Braun J, Lin K, Mclaughlin J, Sprung C, Klingebiel R, & Sack I (2011). In vivo viscoelastic properties of the brain in normal pressure hydrocephalus. NMR in Biomedicine, 24(4), 385–392. 10.1002/nbm.1602 [PubMed: 20931563]

Suga M, Matsuda T, Minato K, Chihara K, Oshiro O, Okamoto J, Takizawa O, Komori M, & Takahashi T (2003). Measurement of In Vivo Local Shear Modulus Using MR Elastography Multiple-Phase Patchwork Offsets. IEEE Transactions on Biomedical Engineering, 50(7), 908–915. 10.1109/TBME.2003.813540 [PubMed: 12848359]

Suga Mikio, Matsuda T, Minato K, Oshiro O, Chihara K, Okamoto J, Takizawa O, Komori M, & Takahashi T (2001). Measurement of in-vivo local shear modulus by combining multiple phase offsets MR elastography. Studies in Health Technology and Informatics, 84, 933–937. 10.3233/978-1-60750-928-8-933 [PubMed: 11604870]

Triolo E, Pionteck A, Alipour A, Khegai O, Kennedy P, Balchandani P, & Kurt M (2021). Development and validation of an ultra-high field compatible MR elastography actuator. Summer Biomechanics, Bioengineering and Biotransport Conference, SB3C2021–325.

Tse ZTH, Janssen H, Hamed A, Ristic M, Young I, & Lamperth M (2009). Magnetic resonance elastography hardware design: A survey. Proceedings of the Institution of Mechanical Engineers, Part H: Journal of Engineering in Medicine, 223(4), 497–514. 10.1243/09544119JEIM529 [PubMed: 19499839]

Uffmann K, Abicht C, Grote W, Quick HH, & Ladd ME (2002). Design of an MR-compatible piezoelectric actuator for MR elastography. Concepts in Magnetic Resonance Part B: Magnetic Resonance Engineering, 15(4), 239–254. 10.1002/cmr.10045

Uffmann K, Abicht C, Quick HH, Ulbrich H, & Ladd ME (2001). Characterization of an Electromagnetic Actuator for MR Elastography. Proc. Intl. Soc. Mag. Reson. Med, 9, 1635. papers://40c68295-5659-4035-8dff-71162e06882b/Paper/p3589

Van Houten EEW, Doyley MM, Kennedy FE, Weaver JB, & Paulsen KD (2003). Initial in vivo experience with steady-state subzone-based MR elastography of the human breast. Journal of Magnetic Resonance Imaging, 17(1), 72–85. 10.1002/jmri.10232 [PubMed: 12500276]

Van Houten EEW, Miga MI, Weaver JB, Kennedy FE, & Paulsen KD (2001). Three-dimensional subzone-based reconstruction algorithm for MR elastography. Magnetic Resonance in Medicine, 45(5), 827–837. 10.1002/mrm.1111 [PubMed: 11323809]

Venkatesh SK, Yin M, & Ehman RL (2013). Magnetic Resonance Elastography of Liver: Technique, Analysis and Clinical Applications. J Magn Reson Imaging, 37(3), 544–555. 10.1002/jmri.23731.Magnetic [PubMed: 23423795]

Wassenaar PA, Eleswarpu CN, Schroeder SA, Mo X, Raterman BD, White RD, & Kolipaka A (2016). Measuring age-dependent myocardial stiffness across the cardiac cycle using MR elastography: A reproducibility study. Magnetic Resonance in Medicine, 75(4), 1586–1593. 10.1002/mrm.25760 [PubMed: 26010456]

Wuerfel J, Paul F, Beierbach B, Hamhaber U, Klatt D, Papazoglou S, Zipp F, Martus P, Braun J, & Sack I (2010). MR-elastography reveals degradation of tissue integrity in multiple sclerosis. NeuroImage, 49(3), 2520–2525. 10.1016/j.neuroimage.2009.06.018 [PubMed: 19539039]

Xu L, Lin Y, Xi ZN, Shen H, & Gao PY (2007). Magnetic resonance elastography of the human brain: A preliminary study. Acta Radiologica, 48(1), 112–115. 10.1080/02841850601026401 [PubMed: 17325935]

Yin M, Manduca A, Romano AJ, Glaser KJ, Drapaca CS, Lake DS, & Ehman RL (2007). 3-D Local Frequency Estimation Inversion for Abdominal MR Elastography. Proc. Intl. Soc. Mag. Reson. Med, 15, 960.

Yin Meng, Rouviere O, Glaser KJ, & Ehman RL (2008). Diffraction-biased shear wave fields generated with longitudinal magnetic resonance elastography drivers. Magnetic Resonance Imaging, 26, 770–780. [PubMed: 18467059]

Yin Z, Kearney SP, Magin RL, & Klatt D (2017). Concurrent 3D acquisition of diffusion tensor imaging and magnetic resonance elastography displacement data (DTI-MRE): Theory and in vivo application. Magnetic Resonance in Medicine, 77(1), 273–284. 10.1002/mrm.26121 [PubMed: 26787007]

Zhang J, Green MA, Sinkus R, & Bilston LE (2011). Viscoelastic properties of human cerebellum using magnetic resonance elastography. Journal of Biomechanics, 44(10), 1909–1913. 10.1016/j.jbiomech.2011.04.034 [PubMed: 21565346]

Zheng Y, Li G, Chen M, Chan QCC, Hu SG, Zhao XN, Ehman RL, Lam EY, & Yang ES (2007). Magnetic resonance elastography with twin pneumatic drivers for wave compensation. Annual International Conference of the IEEE Engineering in Medicine and Biology - Proceedings, 29, 2611–2613. 10.1109/IEMBS.2007.4352864

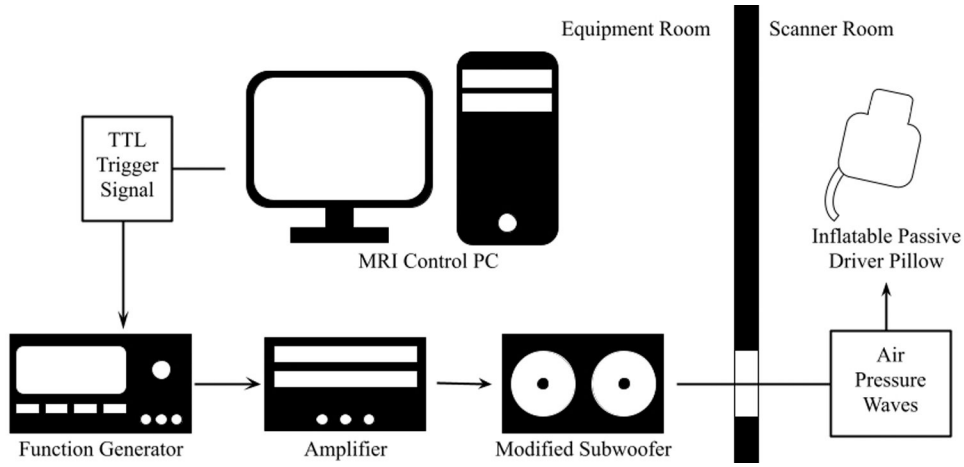

FIGURE 1. MRE Hardware and triggering setup schematic:
The MRI control PC outputs a TTL trigger signal during acquisition that drives a signal generator via external triggering. This in turn sends a pre-determined signal through the amplifier and to the subwoofer, which then pushes air pressure waves through rubber tubing and into the tissue-contacting end-effector.

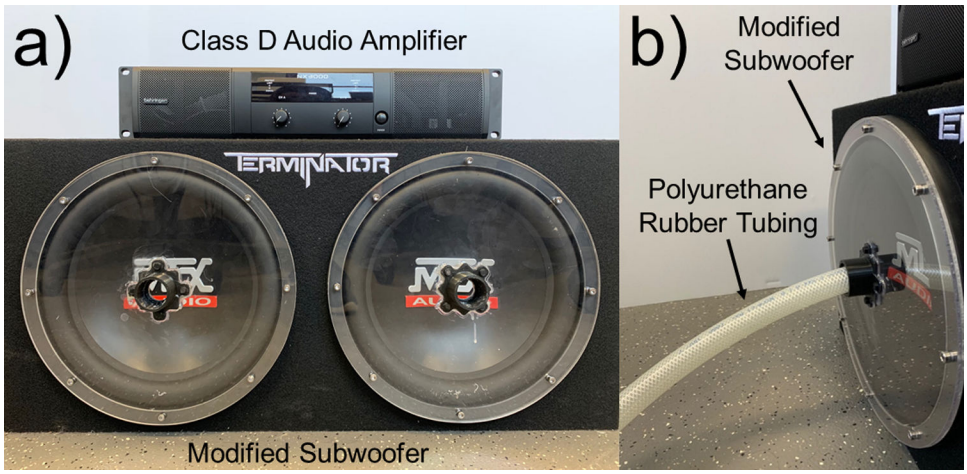

FIGURE 2. Full Active Actuation Component Setup:

The shown components are kept in the equipment room of the MRI scanner. a) the class D audio amplifier selected for our experiments on top of the 12-in dual rubber cone subwoofer modified with acrylic disks over the cones to maintain air pressure, and b) the polyurethane rubber tubing connected to the front of the modified cone to push air pressure waves through the shown tubing into the passive end effector.

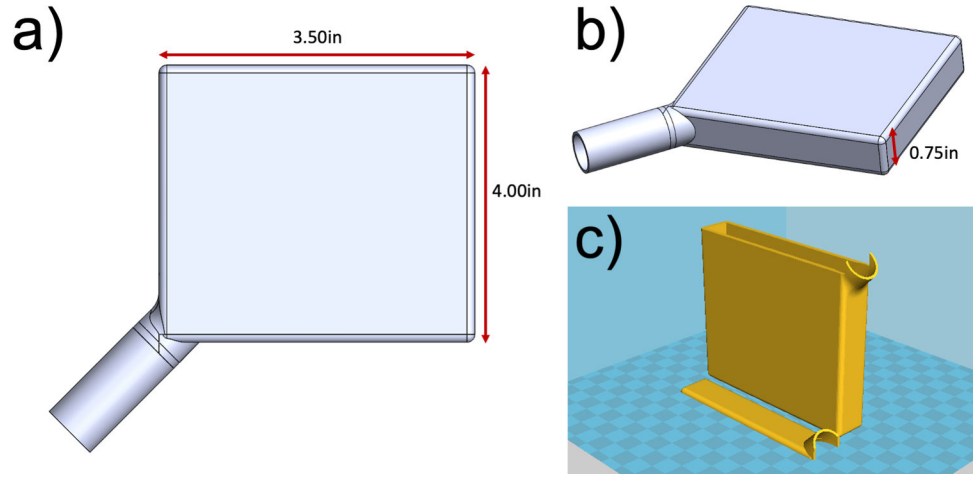

FIGURE 3. Flat End-effector Design:

a) the top and b) isometric views of the 3D CAD model of all the components that make up the flat end-effector design and how they are assembled, and c) how these components are 3D printed in order to keep the end-effector hollow.

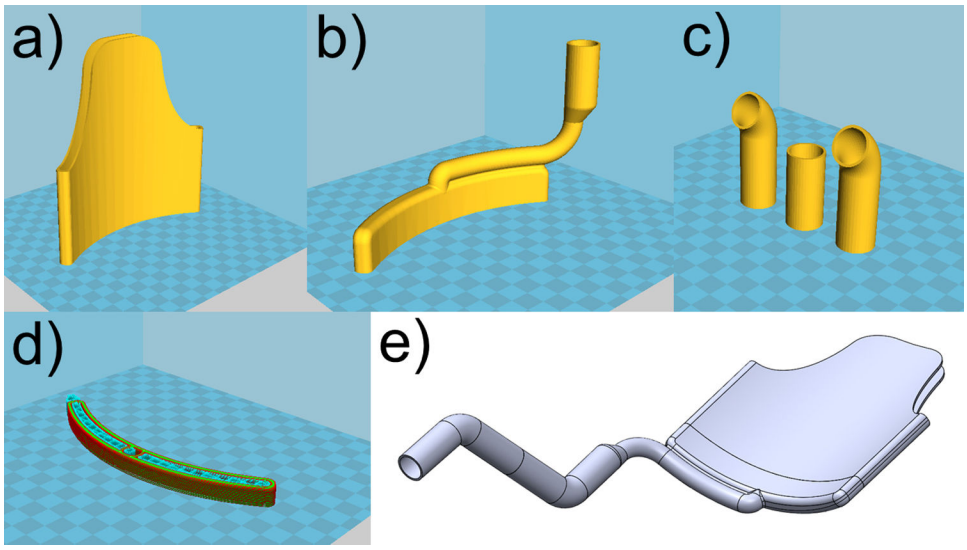

FIGURE 4. Human Brain End-Effector Design:
How the a) main body, b) end cap, and c) tubing bends are 3D printed to manufacture the human brain end-effector such that it remains hollow, despite d) supports added to print the end cap, which can be pulled out once the print has completed. e) How all the 3D printed components are connected together to form the full ‘pillow’.

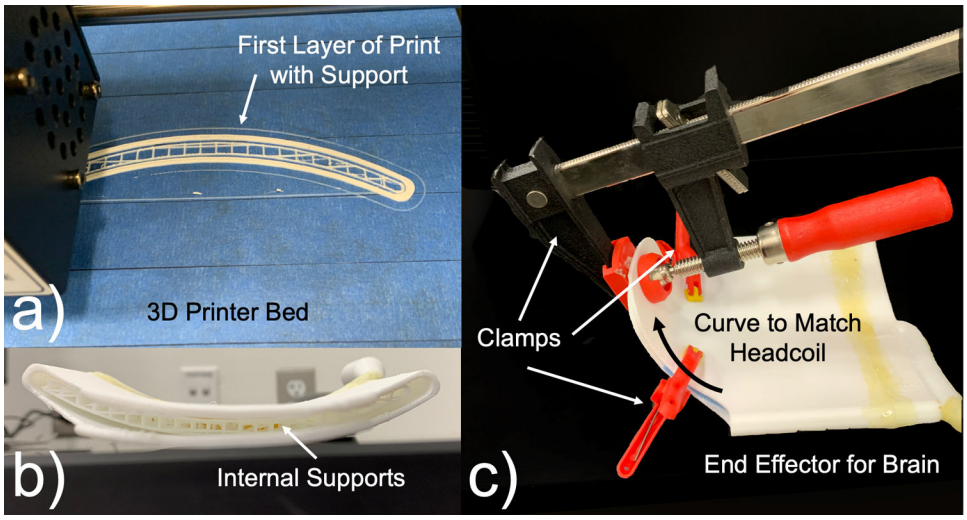

FIGURE 5. Human Brain End-Effector Construction Process:
a) As the end-cap prints, supports are printed along with it to support the top of the cap during printed, and after the supports are removed, b) they are placed inside the main body of the pillow to prevent the weight of the head from fully compressing the pillow during use. c) The separate components are glued together, and the top of the pillow is clamped and glued in a curved shape to match the shape of the head coil.

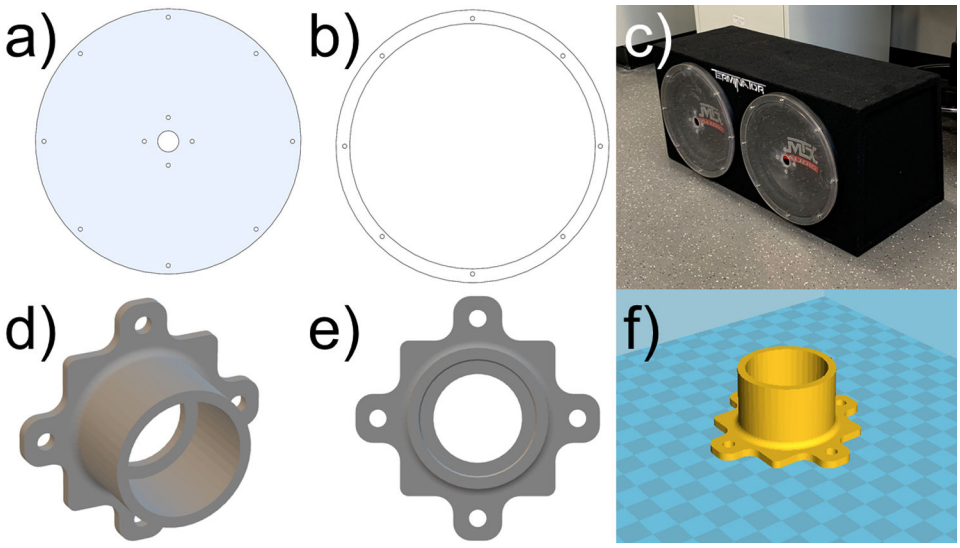

FIGURE 6. Acrylic Disk and Ring, and 3D Printed Tubing Connector:
a) CAD model of the acrylic disk and b) ring that are c) mounted to the front of the subwoofer cones. d) A CAD model of a tubing connector in isometric view and e) front view, and f) how it is 3D printed.

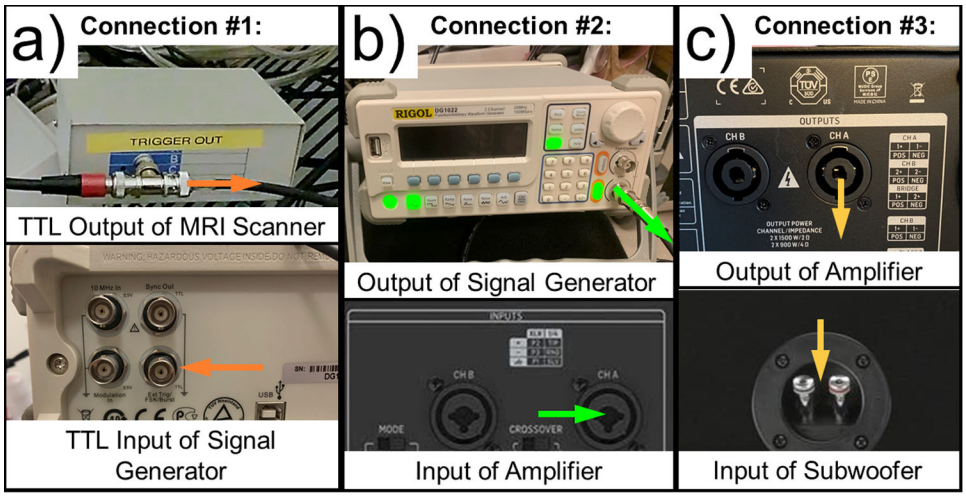

FIGURE 7. Cable Connections:

a) The first cable connection uses a male-male BNC cable to connect the TTL output of the MRI scanner to the TTL external triggering input of the Signal Generator. b) The second connection uses a BNC-male to 3.5mm male cable and a 3.5mm female to 1/4” male adapter to connect the output of the signal generator to the input of the class-D amplifier. c) The third connection uses a Speakon male to Banana male cable to connect the output of the amplifier to the input of the subwoofer.

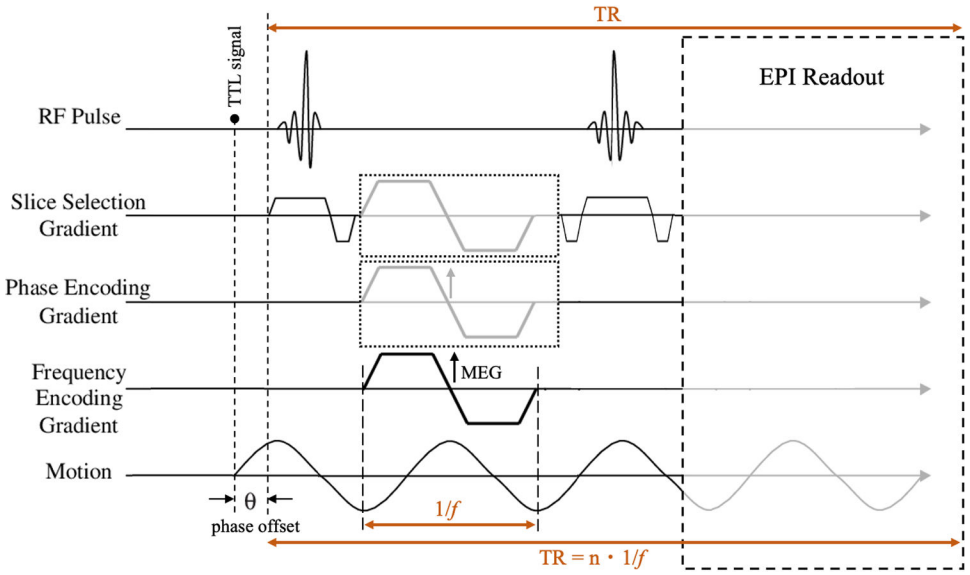

FIGURE 8. Labeled Sequence Diagram:

A 2D EPI multi-slice MRE sequence with 3D motion encoding gradients, labeled with the trigger (TTL) signal, phase offset, vibration period, and true repetition time (TR) labeled.

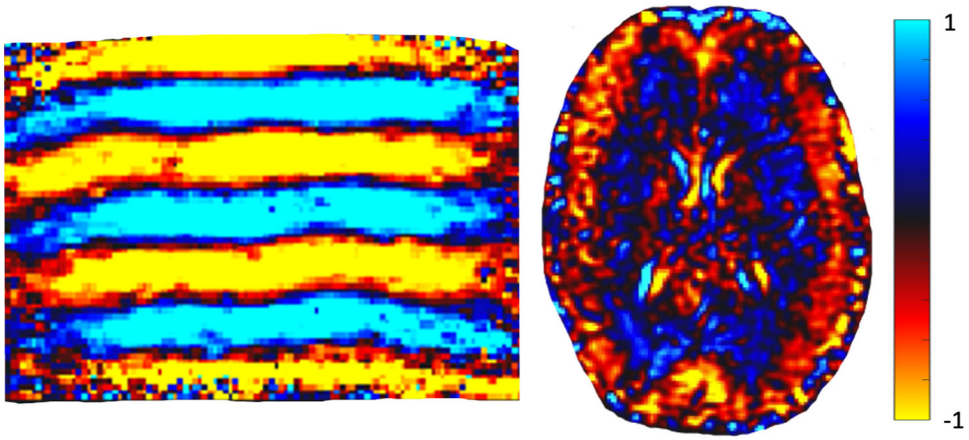

FIGURE 9. Wavefield Images:
of a phantom and human brain captured utilizing a 7T MRE sequence and the actuator described in Basic Protocol 1.

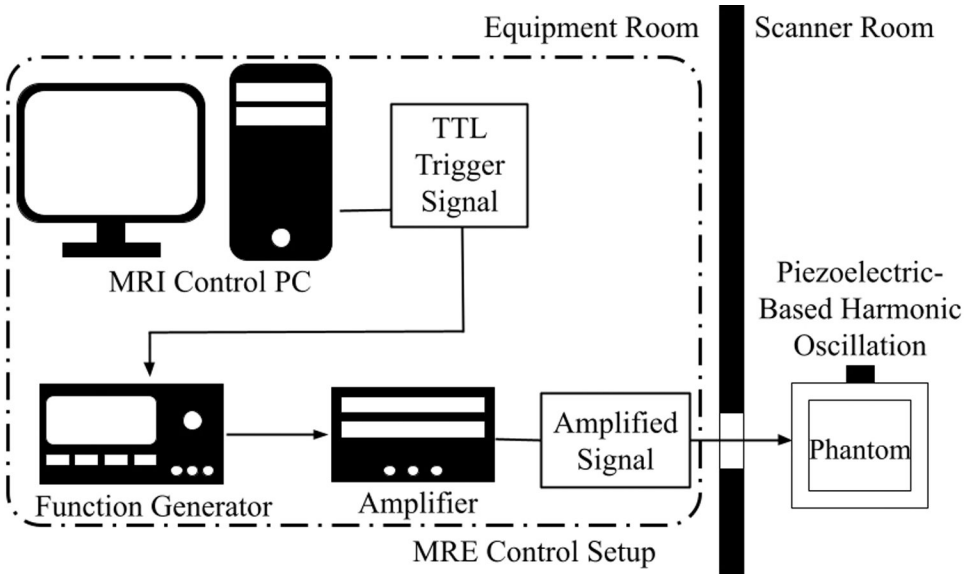

FIGURE 10. Full Piezoelectric Setup Schematic:
The MRE control PC generates a TTL trigger signal to drive the piezoelectric actuator through the amplifier and the function generator via the external trigger input port.

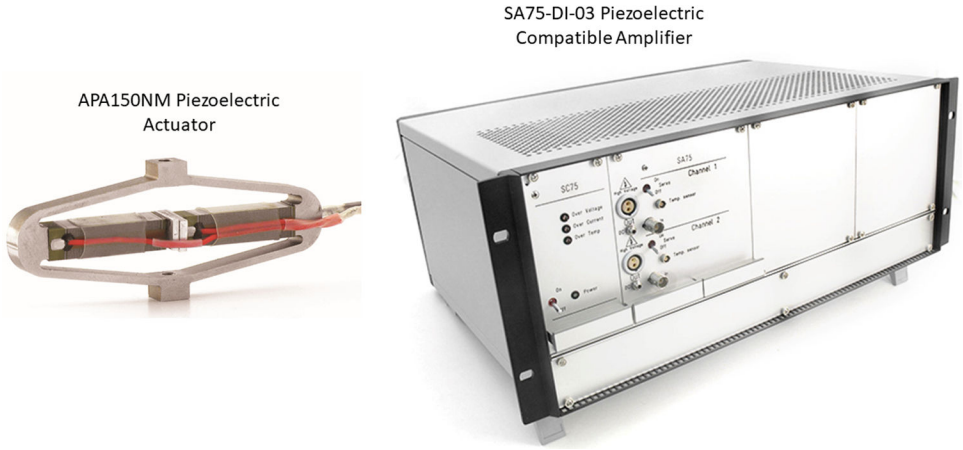

FIGURE 11. CEDRAT Piezoelectric Actuator and Amplifier:
The APA150NM piezoelectric actuator is MRI-safe (NM standing for ‘non-magnetic’), while the compatible amplifier (SA75-DI-03) the actuator is connected to is kept in the scanner’s equipment room.

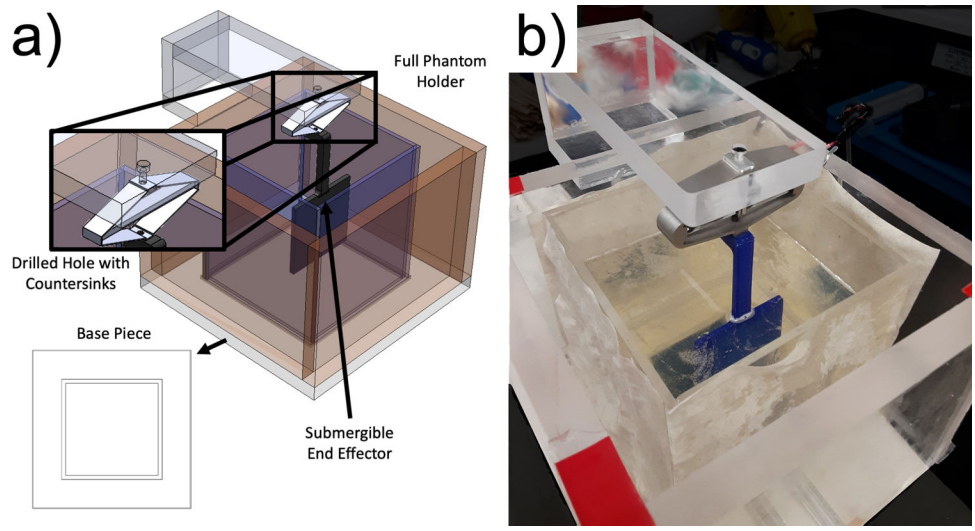

FIGURE 12. Example Phantom Holder Design:

a) The CAD model of the fully constructed phantom holder showing the location of the 0.5” thick outer walls (orange), base (white), and piezoelectric holder parts (gray) with drilled holes, piezoelectric actuator (silver), and 1/8” thick inner walls (purple). The submersible end-effector (black) is screwed to the end of the piezoelectric actuator using a nylon screw, and the phantom material is poured around it into the purple-walled square container. b) Phantom holder with phantom material cured around end effector

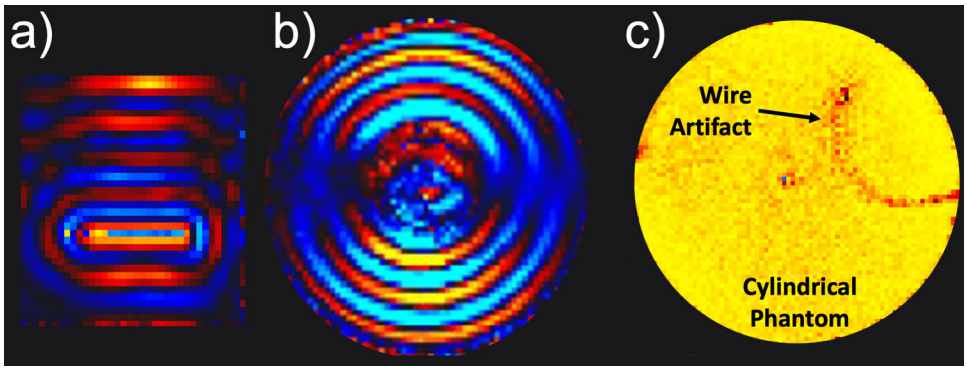

FIGURE 13. Wavefield Images:
obtained utilizing the piezoelectric actuator setup described in Basic Protocol 2 of one phantom in the a) configuration described, and b) one in an alternate cylindrical configuration. c) The cable from the piezoelectric actuator was resting too close to a cylindrical phantom and caused interference in the shape of the cable.

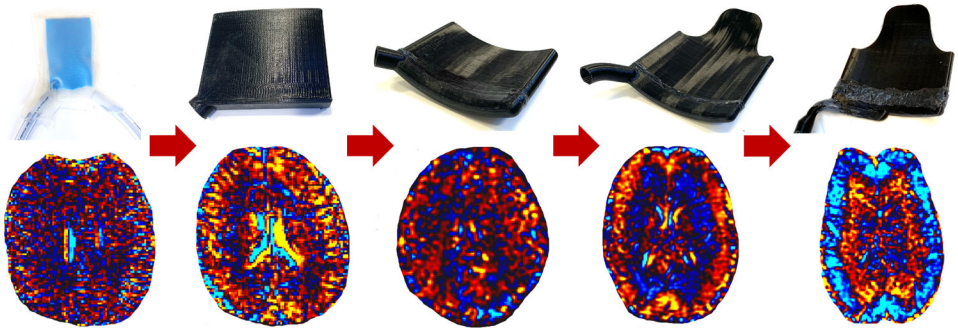

FIGURE 14.

Evolution of the Pneumatic MRE Human Brain end Effector for over time (first through final from left to right), with the corresponding wavefield image below each design.